FINITE ELEMENT SIMULATION OF CRACK DEPTH MEASUREMENTS IN CONCRETE USING DIFFUSE ULTRASOUND

A Thesis
Presented to
The Academic Faculty

by

Matthias E. Seher

In Partial Fulfillment
of the Requirements for the Degree
Master of Science in
Engineering Science and Mechanics

School of Civil and Environmental Engineering
Georgia Institute of Technology
December 2011

FINITE ELEMENT SIMULATION OF CRACK DEPTH MEASUREMENTS IN CONCRETE USING DIFFUSE ULTRASOUND

Approved by:

Dr. Laurence J. Jacobs, Advisor
School of Civil and Environmental Engineering
Georgia Institute of Technology

Dr. Jin-Yeon Kim
School of Civil and Environmental Engineering
Georgia Institute of Technology

Dr. Kimberly Kurtis
School of Civil and Environmental Engineering
Georgia Institute of Technology

Date Approved: August 2011

ACKNOWLEDGEMENTS

This research project could not have been conducted without the help of a large number of people, who provided advise and support in situations of need.

Firstly, I thank Prof. Dr. Laurence Jacobs for making this exchange possible and being a great teacher, supporter and adviser. His endurance in maintaining this exchange program enabled me to gain insight into the world of nondestructive evaluation and elastic wave propagation.

Next, I thank Dr. Jin-Yeon Kim for his advise and the sharing of his knowledge on this research as well as the inspiring discussions. Moreover, I thank Prof. Dr. Kimberly Kurtis for serving on my thesis committee.

Further, I want to express my gratitude towards Prof. Dr. Gaul of the University of Stuttgart for establishing this outstanding exchange program with the Georgia Institute of Technology and making my stay in the USA possible. Moreover, I thank Helge Sprenger and Jan Herrmann from the Institute of Applied and Experimental Mechanics of the University of Stuttgart for the good organization and preparation for this exchange.

I also thank the DAAD (German Academic Exchange Service) for the financial support of this research and my stay at the Georgia Institute of Technology.

I thank my colleagues Kathryn Matlack, Yu Liu, Krzysztof Leśnicki, Chi-Won In, Simon Walker and Christian Ehrlich for their help, friendship and nice working environment. Furthermore, I thank my friends and housemates for their friendship and support.

Finally, I thank my family who always and unconditionally supported me in my adventure at Georgia Tech and the USA.

TABLE OF CONTENTS

LIST OF TABLES

LIST OF FIGURES

LIST OF SYMBOLS

Symbol	Description
b	Forcing condition
$\mathbf{b}$	Vector of nodal forcing conditions of spectral energy source densities
d	Distance between source/receiver and crack
D	Diffusivity coefficient
E	Ultrasonic spectral energy density
E^*	Ultrasonic spectral energy density without dissipation
f	Frequency
i	Index
j	Index
$\mathbf{K}$	Matrix of thermal conductivity
l	Width of rectangular domain
$\mathbf{M}$	Matrix of thermal mass
m	Index
n	Index
P	Spectral energy source density
P_0	Amplitude of spectral energy source density
p	Height of rectangular domain
$\mathbf{Q}$	Vector of external nodal flux of ultrasonic spectral energy density
t	Time
$\mathbf{x}$; x_i	Position vector

Symbol	Description
α	Integer for upper limit of summation
δ	Crack depth
ν	Weighting function
σ	Dissipation coefficient
ϕ	Lagrangian interpolation function

SUMMARY

Surface-breaking cracks pose a serious threat to the service life of concrete structures and health monitoring is presently conducted by a visual inspection method, yielding a potential risk to safety. Diffuse ultrasonic techniques have shown their potential as an ultrasonic technique for measuring crack depth in concrete and are currently under development. In this research, the finite element method (FEM) is employed to model the ultrasound diffusion in a concrete specimen. The objectives are to use the commercial finite element (FE) tool Ansys to develop the finite element model of a concrete specimen and verify the applicability of the model by comparing with an analytic solution and experiment data. Further, various crack types are analyzed with the FE model in order to gain physical insight into the interpretation of experimental measurements.

The results of this research suggest that a preliminary knowledge of the cracking process is required to correctly interpret the measured impulse responses for an unknown crack geometry, as the impulse response expresses the response of the shortest path through a system of cracks between source and receiver. Moreover, the impulse response can carry some ambiguity, as certain crack types are not uniquely determined.

CHAPTER I

INTRODUCTION

1.1 Motivation

All over the world concrete structures are used to span rivers and valleys in order to provide access between cities on the land way. With an ever growing demand for personal mobility, the load on these structures rises and damage may occur, since the structures have been designed for 1950's to 1970's loads. The decline of the performance of service life caused by increasing loads may lead to failure of the concrete structures and poses a risk to public safety as well as financial losses. In order to avoid any lethal incidents, these structures must be inspected regularly and the performance of service life needs to be monitored. For example, in the US, there are a large number of *potentially-defective* bridges that are under health monitoring. One type of critical damage is the presence of surface-breaking cracks, which are presently subjected to visual inspection only, making it impossible to characterize the severity of the crack, as the depth cannot be inspected visually. This type of damage may occur directly throught increasing loads or indirectly as a consequence of other forms of damage. Moreover, low-frequency techniques using, for example Rayleigh waves, are not accurate enough, when the cracks are very shallow (less than $12cm$).

One candidate technique for more quantitative monitoring is a non-destructive evaluation method based on diffuse ultrasound, which is currently under development, in order to achieve more reliable surface breaking crack measurements. For this NDE technique, however, a numerical or analytical model is required to simulate the interaction of the diffuse ultrasonic field with the surface-breaking crack and to determine the crack depth. The finite element method is an established approach

for the numerical modeling of diffuse ultrasound and an additional advantage is its simplicity in application and cost efficiency.

1.2 Literature Review

The topic of diffuse ultrasound has been the subject of research prior to this research. This section intends to give a brief overview of the previous work that has been conducted in the context of this research.

In [13] the propagation of ultrasonic waves in a suspension of glass bead and water is experimentally investigated. The findings show that the diffusion approximation is valid for elastic waves propagating in strongly scattering regimes, in case the wave length is of the order of the scatterers. Moreover, it is found that the diffusivity and dissipation coefficients are independent of the regarded geometry. In [17] the frequency range, for which the diffuse approximation of ultrasonic waves can be applied, is subjected to research in an aluminum foam. The findings show, that for low excitation frequencies the diffusion approximation is invalid and for higher frequencies, when the wave length reaches approximately the strut length of the aluminum foam, the diffusion approximation is applicable. Further, the transitional frequency range between the low and high frequencies is regarded. Cement-based materials are the focus of research in [5], where the diffuse ultrasound approximation is used to characterize the microstructure. The conclusion is that the diffuse ultrasonic approximation can be used for the characterization of cement-based materials with certain restrictions. Finally, in [7], a relationship between the damage state of a cement-based material and the scattering parameters (dissipation and diffusivity coefficients) of cement-based materials is established. The results show that damage causes a change in the microstructure and an increase in the scattering parameters. However, in the previous research, only the microstructural properties are regarded, restricting the diffuse ultrasonic technique to uncracked specimens. In [14] the influence of a

vertical crack on the ultrasound diffusion is studied and a finite element model of the ultrasound diffusion is implemented. The FE model is experimentally validated and the potential for a simulation assisted field application are evaluated, showing that the FE method is a feasible approach.

1.3 Objective

The objective of this research is to develop a finite element model of a concrete specimen with surface-breaking cracks using the commercial FE software Ansys. The FE model is validated by comparing the simulation results to experimental data and an analytic solution. Then, various crack shapes are modeled and the interaction of the diffuse ultrasonic field with the various cracks are analyzed. The investigated crack shapes are:

- vertical cracks relative to the specimen surface
- vertical cracks with a reinforcement bar under the crack tip
- non-vertical cracks caused for example by excessive shear forces
- partially closed cracks accounting for the effect of partial closure due to for example large aggregates
- two closely spaced, vertical and parallel cracks

The simulation results are used to gain physical insight for the interpretation of experimental measurements. Further, the potential to generate a finite element model based look-up table for rapid in-field decision-making is evaluated.

CHAPTER II

THEORY

This chapter deals with the theoretical background of this thesis. First, the theory of ultrasonic energy diffusion will be presented, followed by the finite element formulation of the energy diffusion and the numerical technique used to solve the FE problem.

2.1 Elastic Wave Propagation in Heterogeneous Media

The propagation of waves in a heterogeneous and disordered medium is characterized by a multiple scattering of the incident wave field as it propagates and interacts with scatterers. The process of multiple scattering can be understood as many interactions of a wave field at the interface of two materials with different elastic properties. At the interface, the incident field is partially reflected or transmitted into the second medium. The quantity of the reflected or transmitted part of the wave field is determined by the acoustic impedances of both materials. The acoustic impedance is defined as the mass density of the material multiplied by the phase velocity in the regarded material. Moreover, due to the presence of shear and compression waves in elastic solids, mode conversions can occur at the interface between two materials. In general, the scattering process is regarded as energy conserving. A detailed mathematical illustration of the interaction of elastic waves at material interfaces can be found in for example [1, 9].

In a heterogeneous medium the length scale of the scatterers, the distance between them and wavelength of the propagating wave have a strong influence on the wave propagation. Let R be the distance between the scatterers and the scatterer's size and λ the wavelength of the incident wave, two cases need to be considered according

to [16]. The first is the case when $\lambda >> R$ in which an effective medium approach is applicable as described in [16, 8]. The effective medium is only valid for a small propagation distance and the wave field is partially scattered with increasing propagation distance. In case of $\lambda \approx R$, the effective medium theory is no longer valid and the wave field is characterized by a large number of scattering events, that cause a random behavior of the wave field. In [16] this phenomenon is compared to a random Brownian motion of a particle.

According to [6], in a heterogeneous medium, a ballistic and a diffuse wave field are generated and the total wave field can be regarded as the superposition of these two fields. The ballistic field is mostly uninfluenced by the scatterers or scattered forward and shows a spatially and temporal coherent behavior. The approximation with an effective medium is valid. Moreover, the amplitude of the ballistic field is larger than the amplitude of the later introduced diffuse field. Furthermore, the ballistic field prevails for low frequencies (Rayleigh regime) and low amounts of scatterers. The second field that is generated is the diffuse field and is characterized by the spatial and temporal incoherence. Its origin lies in the vast number of scattering events, that cause the loss of coherence. Furthermore, the direction of propagation is not unique anymore. Another property of the diffuse field is that if it is averaged over a finite volume or a random configuration (distribution of scatterers) it converges to zero. This effect is referred to as phase cancellation [13] and is important in experimental measurement of diffuse fields. Further, the ballistic field does not strongly influence the diffuse field and the evolution of the diffuse field is orders of magnitude slower in time than the ballistic field.

2.1.1 Energy Diffusion and its Approximation

The diffusion approximation of wave fields originates from the study of electromagnetic waves in strongly scattering regimes in the field of astrophysics. In the heterogeneous space, electro-magnetic waves are scattered on cosmic dusts, planets and other cosmic entities. The scattering events cause the electromagnetic wave field to randomize and the field becomes difficult to track. The approach then is to regard the energy evolution of these scattered waves as the wave field itself is too complex. It can then be found that the energy evolves according to the diffusion equation, a second order parabolic partial differential equation. A formal derivation for electromagnetic fields is given in [16].

The major difference between the electromagnetic wave field and an elastic wave field is that the elastic wave field possesses a longitudinal polarization in addition to its two transverse polarizations. However, a conceptually similar approach as in the electromagnetic problem can be taken. In the course of many scattering events, the displacement field can be considered as random. An important assumption that needs to be made at this point is that there is neither spacial nor temporal coherence in the wave field. This makes it possible to treat the wave field on an energy basis rather than based on the displacement field. The evolution of the energy is then governed by the diffusion equation. Nevertheless, the diffusion equation represents an approximation of the behavior of the strongly scattered elastic wave field leading to the question on the quality of the approximation. The first limitation to the diffusion approximation is the minimum distance that is necessary to consider the wave field fully randomized. This distance is analyzed for example in [18] for a suspension of glass beads in water and it is found that the minimum distance necessary is about four to ten scattering mean free path. The scattering mean free path can be understood as the distance of propagation of a wave between two scattering events. However, this result applies only for the given experimental setup of Zhang et al. [18], as

this distance depends on various factors such as for example the scatterer density or distribution. Another limitation is the frequency range, which is directly correlated with the wavelength and hence the scatterer size, yielding that higher frequencies behave more diffusely than lower frequencies. The reason for this can be found in the fact that a wavelength on the order of the scatterers are scattered more than longer wavelengths, as mentioned earlier. In [17], Weaver for example identifies three frequency ranges. The low frequency range is characterized by the mean free path going to infinity (Rayleigh regime), where as the higher frequency range has a mean free path of the size of the scatterers (in Weaver's case the length of the struts of the aluminum foam structure). The intermediate frequency range is the transition of the mean free path from infinity to the size of the scatterers.

The equation for the ultrasound diffusion can be derived with either a random walk model (an approach similar to the derivation of heat transfer [12]) or established by regarding the ultrasound diffusion as quantum mechanical problem [16]. In order to establish the ultrasound diffusion equation several assumptions are made (see also [5, 8]). It is assumed that the scatterers are randomly distributed in the elastic solid and no resonance effects occur due to periodic distributions. Moreover, the scattering process is linear elastic, which means that no energy is lost during the interaction of the wave field with the scatterer. Furthermore, no change in frequency is assumed during the scattering process (linearity). The diffusion equation can then be written as

$$\frac{\partial}{\partial t}\langle E(\mathbf{x},t,f)\rangle - D\nabla^2\langle E(\mathbf{x},t,f)\rangle + \sigma\langle E(\mathbf{x},t,f)\rangle = P(\mathbf{x},t,f), \quad \forall \mathbf{x} \in \mathcal{B}, \tag{2.1}$$

which represents a second order parabolic partial differential equation (PDE). In Equation (2.1), $\langle E(\mathbf{x},t,f)\rangle$ represents the spectral energy density per unit volume and frequency. The $\langle\cdot\rangle$ operator indicates an expected value as the distribution of the scatterers in the disordered medium is probabilistic. Moreover, the term $P(\mathbf{x},t,f)$ illustrates the spectral source energy density, which is the excitation term of the PDE.

The coefficients D the diffusivity and σ the dissipation are the scattering properties of the arbitrarily shaped medium $\mathcal{B}$ under consideration.

2.1.1.1 Diffusivity Coefficient

The diffusion coefficient $D(f)$ is a frequency dependent material parameter. It has the unit $[m^2 s^{-1}]$ and determines the diffusion rate of the ultrasonic field. Higher values correspond to faster diffusion.

2.1.1.2 Dissipation Coefficient

The dissipation coefficient $\sigma(f)$ is a material parameter that represents the rate of loses of energy due to for example internal friction. It can be found that the loses due to dissipation are of temporal nature and do not depend on the location $\mathbf{x}$ in the medium. The unit of dissipation is $[s^{-1}]$. The frequency dependent dissipation is not to be mistaken with the acoustic attenuation which also accounts for the reduction of the wave amplitude due to the geometric attenuation for example in a 2D domain due to a point source.

2.1.2 Analytical Solutions to the Diffusion Equation

An analytical solution can be found for Equation (2.1) by applying appropriate boundary and initial conditions. The initial condition is assumed to be

$$\langle E(\mathbf{x}, 0, f)\rangle = 0, \quad \forall \mathbf{x} \in \mathcal{B}, \tag{2.2}$$

which means that the diffuse ultrasonic energy is zero initially, hence the medium $\mathcal{B}$ is at "rest". For the boundary conditions, it is assumed that there is no flux across the surface of the medium $\partial\mathcal{B}$ so that

$$\nabla\langle E(\mathbf{x}, t, f)\rangle = 0, \quad \forall \mathbf{x} \in \partial\mathcal{B}. \tag{2.3}$$

This kind of boundary conditions originates from the assumption that there is a high mechanical impedance mismatch between the regarded medium $\mathcal{B}$ and the surrounding medium such as for example air.

In the following, Equation (2.1) is solved analytically for two-dimensional cases.

2.1.2.1 Impulse Response of a Bounded 2D Domain

The solution for Equation (2.1) is given for a rectangular domain $\mathcal{B}$ in a Cartesian space that extends in two dimensions x_1 and x_2. The forcing term is given by $P(\mathbf{x}, t) = P_0\delta(t)\delta(\mathbf{x} - \mathbf{x_0})$ with P_0 being the height of the impulse and $\mathbf{x_0}$ the location of the excitation. Moreover, it is assumed that the gradient in the third dimension is equal to zero, which means that there is no change in that direction of the ultrasonic energy. After applying the initial (Equation (2.2)) and boundary (Equation (2.3)) conditions the solution can be written, as in [14], as

$$\begin{aligned}\langle E(\mathbf{x}, t, f)\rangle = \quad & \Bigg\{1 + \sum_{n=1}^{\infty} 2\cos\left(\frac{n\pi x_{1,0}}{l}\right)\cos\left(\frac{n\pi x_1}{l}\right)e^{-D(\frac{n\pi}{l})^2 t} \\ & + \sum_{m=1}^{\infty} 2\cos\left(\frac{m\pi x_{2,0}}{p}\right)\cos\left(\frac{m\pi x_2}{p}\right)e^{-D(\frac{m\pi}{p})^2 t} \\ & + \sum_{n=1}^{\infty}\sum_{m=1}^{\infty} 4\cos\left(\frac{n\pi x_{1,0}}{l}\right)\cos\left(\frac{n\pi x_1}{l}\right)\cos\left(\frac{m\pi x_{2,0}}{p}\right)\cos\left(\frac{m\pi x_2}{p}\right) \\ & \times e^{-D[(\frac{n\pi}{l})^2 + (\frac{m\pi}{p})^2]t}\Bigg\} \\ & \times P_0 e^{-\sigma t}, \quad \mathbf{x} \in \mathcal{B}.\end{aligned} \tag{2.4}$$

In Equation (2.4) the variables l and p denote the spacial extend of the rectangular domain $\mathcal{B}$. The variables $x_{1,0}$ and $x_{2,0}$ represent the location of impulse excitation and x_1 and x_2 depict the location of the receiver. A parameter study on the influence of the diffusivity D and the dissipation σ on the energy versus time behavior has been conducted in [14].

2.2 Finite Element Formulation

The finite element method (FEM) is a numerical technique with which partial differential equations can be solved numerically. Unlike the analytical solution, the FEM yields only an approximation of the solution to the problem. The major advantage of the FEM is that complex geometries, initial and boundary conditions can be easily treated. The idea of FEM is to discretize a continuous system with an infinite number of degrees of freedom to a discrete system with a finite number of degrees of freedom such that the discretization error is small.

2.2.1 Derivation of the Element Matrices

In this section the finite element equations are derived for a two dimensional domain. Further, the dependencies of the various variables are neglected. Starting off with the PDE for the ultrasonic energy diffusion (also see Equation (2.1)),

$$\dot{E} - D\nabla^2 E + \sigma E - b = 0 \tag{2.5}$$

the integral form given by multiplying with a weighting function ν and integrating over one element Ω_e can be written as

$$\int_{\Omega_e} \nu\big(\dot{E} - D\nabla^2 E + \sigma E - b\big) dA = 0. \tag{2.6}$$

In Equations (2.5) and (2.6) the variable b represents the forcing condition. By multiplying ν into the integrand and applying the Laplacian operator, Equation (2.6) then reads

$$\int_{\Omega_e} \big(\nu\frac{\partial E}{\partial t} - D\nu\frac{\partial^2 E}{\partial x_1^2} - D\nu\frac{\partial^2 E}{\partial x_2^2} + \nu\sigma E - \nu b\big) dA = 0. \tag{2.7}$$

Equation (2.7) contains two second order derivatives of which one can be traded onto ν by applying the product rule

$$\frac{\partial}{\partial x_i}\left[\nu\frac{\partial E}{\partial x_i}\right] = \nu\frac{\partial^2 E}{\partial x_i^2} + \frac{\partial \nu}{\partial x_i}\frac{\partial E}{\partial x_i}, \tag{2.8}$$

such that

$$\nu \frac{\partial^2 E}{\partial x_i^2} = \frac{\partial}{\partial x_i}\left[\nu \frac{\partial E}{\partial x_i}\right] - \frac{\partial \nu}{\partial x_i}\frac{\partial E}{\partial x_i} \tag{2.9}$$

with i representing the index of the respective spacial directions. Plugging Equation (2.9) into Equation (2.7) then yields the weak form of the PDE

$$\begin{aligned} &\int_{\Omega_e} \left(\nu \frac{\partial E}{\partial t} + D\left(\frac{\partial \nu}{\partial x_1}\frac{\partial E}{\partial x_1} + \frac{\partial \nu}{\partial x_2}\frac{\partial E}{\partial x_2}\right) + \nu\sigma E\right) dA = \\ &\int_{\Omega_e} \left(\frac{\partial}{\partial x_1}\left[D\nu \frac{\partial E}{\partial x_1}\right] + \frac{\partial}{\partial x_2}\left[D\nu \frac{\partial E}{\partial x_2}\right] + \nu b\right) dA \end{aligned} \tag{2.10}$$

The divergence theorem [15]

$$\int_A \frac{\partial g_i}{\partial x_i}\, dA = \int_A \nabla \cdot \mathbf{g}\, dA = \oint_{\partial A} \mathbf{g} \cdot \mathbf{n}\, ds = \oint_{\partial A} g_i n_i\, ds \tag{2.11}$$

can be used to further simplify the weak from by converting the area integrals of the first two terms of the right hand side of Equation (2.10) to a boundary integral. In Equation (2.11) the variable $\mathbf{n}$ or n_i denote the outward normal vector on the surface ∂A. Moreover, the divergence theorem is given in index notation representation. The simplified weak form then reads

$$\begin{aligned} &\int_{\Omega_e} \left(\nu \frac{\partial E}{\partial t} + D\left(\frac{\partial \nu}{\partial x_1}\frac{\partial E}{\partial x_1} + \frac{\partial \nu}{\partial x_2}\frac{\partial E}{\partial x_2}\right) + \nu\sigma E\right) dA = \\ &\int_{\Omega_e} \nu b\, dA + \oint_{\Gamma_e} \nu D\left(\frac{\partial E}{\partial x_1} n_1 + \frac{\partial E}{\partial x_2} n_2\right) ds \end{aligned} \tag{2.12}$$

with Γ_e representing the boundary of the element Ω_e with the normal vector components n_1 and n_2. The solution for E of the regarded element Ω_E can be approximated by

$$E = \sum_{i=1}^{k} E_i \psi_i = E_i \psi_i. \tag{2.13}$$

In Equation (2.13) the variable E denotes the spectral energy density at a given location within the element, whereas E_i represents the nodal value of node i of the element with k nodes in total. Moreover, ψ_i depicts a member of the Lagrange family of interpolation functions [15]. Furthermore, it should be noticed that in Equation (2.13) E_i does not show any spacial and ψ_i any temporal dependency.

Finally, by employing the Rayleigh-Ritz technique ($\nu = \psi_j$) and plugging Equation (2.13) into Equation (2.12) the element equations of the finite element formulation for one element of the PDE of Equation (2.5) can be written as

$$\begin{aligned}\int_{\Omega_e} \psi_j \psi_i \; dA \; \dot{E}_i + \int_{\Omega_e} \left(D \frac{\partial \psi_j}{x_1} \frac{\partial \psi_i}{x_1} + D \frac{\partial \psi_j}{x_2} \frac{\partial \psi_i}{x_2} + \sigma \psi_j \psi_i \right) dA \; E_i = \\ \oint_{\Gamma_e} \psi_j D \left(\frac{\partial E}{\partial x_1} n_1 + \frac{\partial E}{\partial x_2} n_2 \right) ds + \int_{\Omega_e} \psi_j b \; dA.\end{aligned} \tag{2.14}$$

Equation (2.14) represents a set of k equations and can be also illustrated in matrix form

$$\mathbf{M^E} \cdot \dot{\mathbf{E}} + \mathbf{K^E} \cdot \mathbf{E} = \mathbf{Q^E} + \mathbf{b^E}, \tag{2.15}$$

with the integrals of Equation (2.14) representing the various terms with superscript E. In Equation (2.15) $\mathbf{M^E}$ and $\mathbf{K^E}$ represent the thermal mass and conductivity matrix of the element. The variables $\mathbf{Q^E}$ and $\mathbf{b^E}$ denote the external nodal flux and the nodal forcing condition. By applying the boundary conditions of Equation (2.3) and the fact that there is no external nodal energy flux into the element, the term $\mathbf{Q^E}$ becomes zero. The final version of the element equations the is given by

$$\mathbf{M^E} \cdot \dot{\mathbf{E}} + \mathbf{K^E} \cdot \mathbf{E} = \mathbf{b^E} \tag{2.16}$$

as also obtained in [14].

Another way to perceive the ultrasonic diffusion Equation (2.1) is to view it as a modified heat conduction PDE as the dissipation term $\sigma \langle E(\mathbf{x}, t, f) \rangle$ does not complicate the solution. With the ansatz

$$\langle E(\mathbf{x}, t, f) \rangle = \langle E^*(\mathbf{x}, t, f) \rangle e^{-\sigma t}, \tag{2.17}$$

the dissipation term can be eliminated from the ultrasonic diffusion equation by plugging it into the unexcited ultrasonic diffusion equation

$$\frac{\partial}{\partial t} \langle E(\mathbf{x}, t, f) \rangle - D \nabla^2 \langle E(\mathbf{x}, t, f) \rangle + \sigma \langle E(\mathbf{x}, t, f) \rangle = 0, \quad \forall \mathbf{x} \in \mathcal{B}. \tag{2.18}$$

This yields the dissipation free ultrasonic diffusion equation

$$\frac{\partial}{\partial t}\langle E^*(\mathbf{x},t,f)\rangle - D\nabla^2\langle E^*(\mathbf{x},t,f)\rangle = 0, \quad \forall \mathbf{x} \in \mathcal{B}. \tag{2.19}$$

In Equations (2.17) and (2.19) the term $\langle E^*(\mathbf{x},t,f)\rangle$ denotes the spectral energy density per unit volume and frequency without dissipation. One can easily see that Equation (2.19) is the well known heat conduction equation as illustrated in [12] or in [11] if thermal wave fields are regarded. The decoupling of the dissipation term therefore enables the usage of the finite element modeling approach for thermal problems. Moreover, as illustrated in Equation (2.4), the dissipation can then be accounted for after a FE simulation run by simple multiplication. The derivation of the element equations for the decoupled problem is the same as for the approach when regarding the dissipation term. The only difference is that all terms containing σ need to be set equal to zero. A formal derivation of the element matrices for the heat conduction equation can be found in [4, 15]. The advantage of the decoupling is that commercial FE tools can be used in order to model the energy diffusion in disorded media rather than developing an own element type as in [14] to treat the dissipation.

2.2.2 Numerical Solution of FE Problems

Over time many techniques have been developed to solve Equation (2.16) numerically. In this section the technique used by the commercial FE tool Ansys is described, which is also illustrated in the documentation [2].

For the solution of transient thermal problems Ansys uses the Newmark algorithm to solve Equation (2.16). This equation can be rewritten for every integration step during the numerical integration of Equation (2.16) as

$$\mathbf{M}\cdot\dot{\mathbf{E}}^{n+1} + \mathbf{K}\cdot\mathbf{E}^{n+1} = \mathbf{b_n}. \tag{2.20}$$

with n being the current integration step. The index E has been removed compared to Equation (2.16) as now the global assembly matrices are regarded. The backwards

Euler method

$$\dot{\mathbf{E}}^{n+1} = \frac{\mathbf{E}^{n+1} - \mathbf{E}^{n}}{\Delta t} \tag{2.21}$$

is used to approximate the time derivative of the ultrasonic spectral energy density for every integration step $n+1$ with Δt being the time step size. After plugging Equation (2.21) into (2.20), the update equation for the ultrasonic spectral energy density can be obtained as

$$\left[\frac{1}{\Delta t}\mathbf{M} + \mathbf{K}\right]\mathbf{E}^{n+1} = \mathbf{b_n} + \mathbf{K}\left[\frac{1}{\Delta t}\mathbf{E}^{n} + \dot{\mathbf{E}}^{n}\right]. \tag{2.22}$$

Equation (2.22) represents a linear system of equations with the unknown $\mathbf{E}^{n+1}$. The time derivative of $\dot{\mathbf{E}}^{n+1}$ for the integration step $n+1$ can be obtained by employing Equation (2.21). Moreover, the matrices $\mathbf{M}$ and $\mathbf{K}$ are symmetric and according to the Ansys documentation [2] this algorithm is unconditionally stable for all Δt. In order to improve the convergence speed for a demanded accuracy, this algorithm offers a step size control.

CHAPTER III

FINITE ELEMENT MODELING

This chapter deals with the modeling process of the ultrasound diffusion experiments. First, the general modeling approach is presented and the model is validated on basis of the analytical solution. Further, in this chapter, the models used in this research are illustrated.

3.1 General Modeling Approach

This research uses the commercial finite element software tool Ansys (or Ansys Classic) in order to conduct the numerical simulations. Ansys is a commonly used FE tool in research and development in academia as well as in industrial applications. It features a broad variety of models reaching from electromagnetic field analysis over stress analysis to thermal and coupled field analysis just to name a few.

The starting point for the modeling process of this research is the concrete specimen used for experimental testing, which is illustrated in Figure 3.1. The specimen is a cuboid block of concrete with the dimensions depicted in Table 3.1. The geometry for the simulation model is derived from the concrete block by regarding the vertical symmetry plane with the side dimensions of height and width (see Table 3.1). However, the dimensions for the geometry have been slightly modified, such that the width is $0.6m$ and a height of $0.25m$. This approach has also been taken

Table 3.1: Dimensions of concrete block.

Parameter	Height	Width	Depth
Dimension	615 mm	254 mm	325 mm

Figure 3.1: Concrete block.

by Turner in [14]. Based on the rectangular two-dimensional geometry the FE model is generated. For the modeling of the geometry a bottom-up modeling approach is chosen, which means that, first, the vertices (key points in Ansys) of the geometry are generated at their respective locations in the global coordinate frame. From the vertices, the lines and then the area are created. As discussed in the last chapter, the ultrasonic diffusion equation can be transformed to the heat equation enabling one to use the modeling approach for heat conduction problems. Out of that reason, the finite element mesh is generated on the area using bilinear quadrilateral elements of the type "plane55" in Ansys. The "plane55" element has four nodes with one degree of freedom at each node. Further information on this element type can be found in the Ansys documentation [2]. In Figure 3.2 the FE model of the concrete block (Figure 3.1) is illustrated and the global coordinate system based on which the model

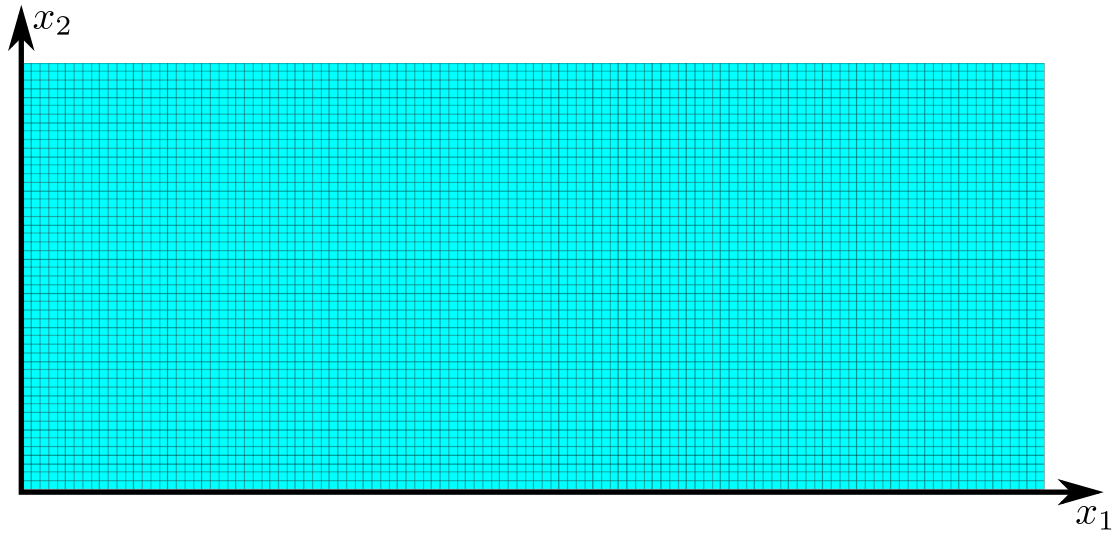

Figure 3.2: FE model of concrete block.

is defined is given.

With the approach of a thermal modeling of the ultrasonic diffusion process, the thermal material properties (mass density, conductivity and specific heat) need to be adapted in order to account for the ultrasonic diffusion properties. This is achieved by setting the thermal material parameters as depicted in Table 3.2, with D being the ultrasonic diffusivity. The units have been neglected in Table 3.2 as the thermal problem units do not apply to the ultrasonic diffusion units. Nevertheless, the SI unit system is used for the whole modeling process including the modeling of the geometry. This is possible because Ansys does not specify or demand any unit system.

Table 3.2: Thermal material properties to model ultrasonic diffusion.

Parameter	Mass density ρ	Conductivity λ	Specific heat c_p
Value	1.0	D	1.0

3.1.1 Ultrasonic Material Properties

The ultrasonic material parameters in this research are obtained from the experimental measurements on the specimen shown in Figure 3.1 using the analytical solution

Table 3.3: Diffusivity and dissipation parameters at 500KHz for the simulations.

Parameter	Diffusivity D	Dissipation σ
Value	$10\frac{m^2}{s}$	$21000\frac{1}{s}$

for a bounded two-dimensional domain given in Equation (2.4). This approach is also used by [8]. The values for the diffusivity and dissipation that are used in the simulations are given in Table 3.3.

3.1.2 Model Excitation

The excitation of the FE model is modeled as a heat generation on the node that is to be excited. This modeling approach also fulfills the partial differential Equation (2.1) and is hence valid. Further, the excitation is assumed to be an impulse, which needs to be numerically approximated. The impulse is approximated by two step functions with a step height of the source spectral energy density P_0 and a pulse duration of Δt. The duration of the impulse is chosen as $100ns$ and the height P_0 is selected specific to the problem, but ranging around 10^9 in magnitude.

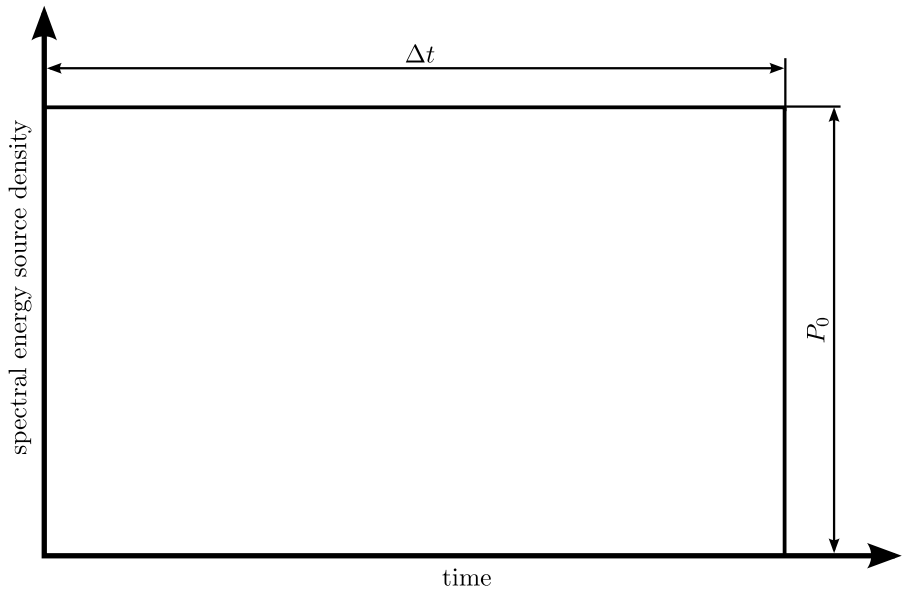

Figure 3.3: Shape of the numerical impulse used to excite the FE model.

3.1.3 Initial and Boundary Conditions

The boundary conditions for the FE model are implemented as described in Equation (2.3), which means that the boundary flux of the elements is zero. Moreover, the initial conditions are assumed to be zero, as there is no ultrasonic energy in the domain at time zero.

3.1.4 Numerical Integration

The numerical integration in Ansys for transient thermal problems, such as in this research, uses the integrator, which is described in Section 2.2.2. This integrator features a step size control, in order to improve accuracy and computational effort. For the numerical integration an initial step size of $10ns$ is chosen to get sufficient temporal resolution during the excitation of the model. Later a maximum step size of $1\mu s$ is allowed to capture the diffusion process accurately.

3.2 Software Architecture

With the goal to increase the efficiency of the simulations, the whole simulation process has been engineered in such a way, that multiple tests can be easily conducted on one simulation model. The software tool Matlab by Mathworks delivers the necessary features to meet this goal and is used to run the simulations as well as to analyze the results afterwords. Therefore, the simulation process is split up into two separate steps with, first, the simulation step and then followed by the evaluation step of the simulation results. The simulation step is depicted in Figure 3.4, which shows the work flow of the employed software tools. First, with Matlab the simulation parameters are initialized and the Ansys input file is generated. Next, Ansys is called from Matlab and a simulation run with the generated input file is conducted. The results of the Ansys simulation run are then stored in a text file, which is loaded into Matlab again. After accounting for the dissipation in Matlab, the data is stored in a structure

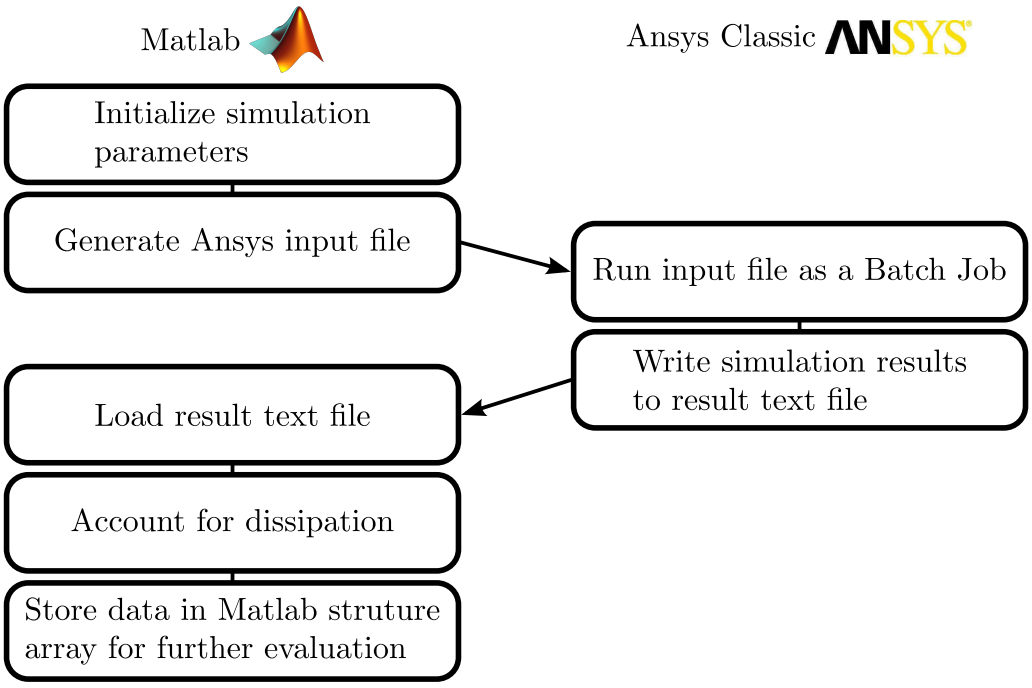

Figure 3.4: Software architecture of the simulation step of the simulation process.

array. This yields the advantage that all the simulation runs for each test case are condensed in one file, which can then be evaluated further in the evaluation step.

3.3 Convergence Test of FE Model

The purpose of the convergence test is to analyze the applicability of the FE model and to determine the number of elements that are necessary to achieve the required accuracy of the model. For this analysis, the result of the FE simulation, namely the ultrasonic spectral energy density versus time behavior to an impulse excitation, is compared with the analytical solution of the problem under variation of the number of elements. The FE model employed for the convergence test is the model depicted in Figure 3.2 and the analytical equation is given by Equation (2.4).

3.3.1 Convergence of Analytical Solution

The analytical solution for a rectangular domain, as given in Equation (2.4), contains summations from 1 to ∞. For the numerical treatment, although, the upper limit for

the summation needs to be finite and therefore the question of what should be the upper limit for the summation in order to attain sufficient accuracy of the analytical solution needs to be answered. This problem can be understood as a convergence test for the analytical solution itself. For the convergence analysis, the analytical solution (Equation (2.4)) can be split up into three different sums,

$$\Sigma_{m=1}^{\alpha}(...) = \sum_{m=1}^{\alpha} 2\cos\left(\frac{m\pi x_{2,0}}{p}\right)\cos\left(\frac{m\pi x_2}{p}\right)e^{-D(\frac{m\pi}{p})^2 t}e^{-\sigma t}, \tag{3.1}$$

$$\Sigma_{n=1}^{\alpha}(...) = \sum_{n=1}^{\alpha} 2\cos\left(\frac{n\pi x_{1,0}}{l}\right)\cos\left(\frac{n\pi x_1}{l}\right)e^{-D(\frac{n\pi}{l})^2 t}e^{-\sigma t} \tag{3.2}$$

and

$$\begin{aligned}\Sigma_{m=1}^{\alpha}\Sigma_{n=1}^{\alpha}(...) = \quad & \sum_{n=1}^{\alpha}\sum_{m=1}^{\alpha} 4\cos\left(\frac{n\pi x_{1,0}}{l}\right)\cos\left(\frac{n\pi x_1}{l}\right)\cos\left(\frac{m\pi x_{2,0}}{p}\right)\cos\left(\frac{m\pi x_2}{p}\right) \\ & \times e^{-D[(\frac{n\pi}{l})^2+(\frac{m\pi}{p})^2]t}e^{-\sigma t},\end{aligned} \tag{3.3}$$

capturing the terms relevant for convergence. This is possible even though the analytical solution contains four terms, as the first term is constant or converges to zero due to the multiplication with $e^{-\sigma t}$. Moreover, the variable P_0 is set to one without any loss of generality. Finally regarding α as a variable, each of the three sums from 1 to α can be interpreted as a series for which the convergence can be investigated. The results for each sum is illustrated in Figure 3.5. From Figure 3.5a it can be clearly seen, that the series $\Sigma_{m=1}^{\alpha}(...)$ converges for an increasing α, if the time t is greater than zero, as for $t = 0$ the series diverges. The second series $\Sigma_{n=1}^{\alpha}(...)$ shows a similar behavior as the first series ($\Sigma_{m=1}^{\alpha}(...)$), convergence for an increasing α. Moreover, for $t = 0$ the sum does not converge either. The last sum ($\Sigma_{m=1}^{\alpha}\Sigma_{n=1}^{\alpha}(...)$) is the product of the first two and therefore shows a converging behavior with increasing α and diverges for $t = 0$. Furthermore, for higher values of t the summands necessary until convergence decreases, which can easily observed from Figures 3.5a, 3.5b and 3.5c. In order to be a valid model for the convergence test of the finite element simulation

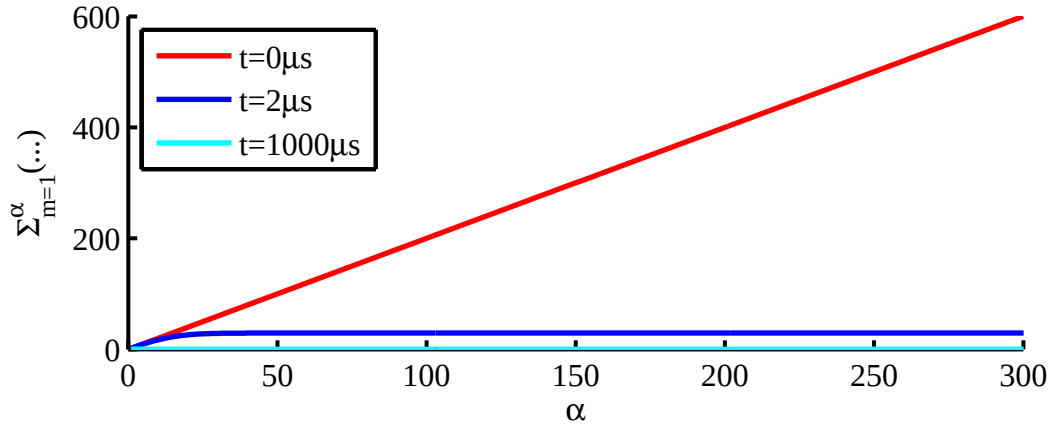

(a) Plot of Equation (3.1)

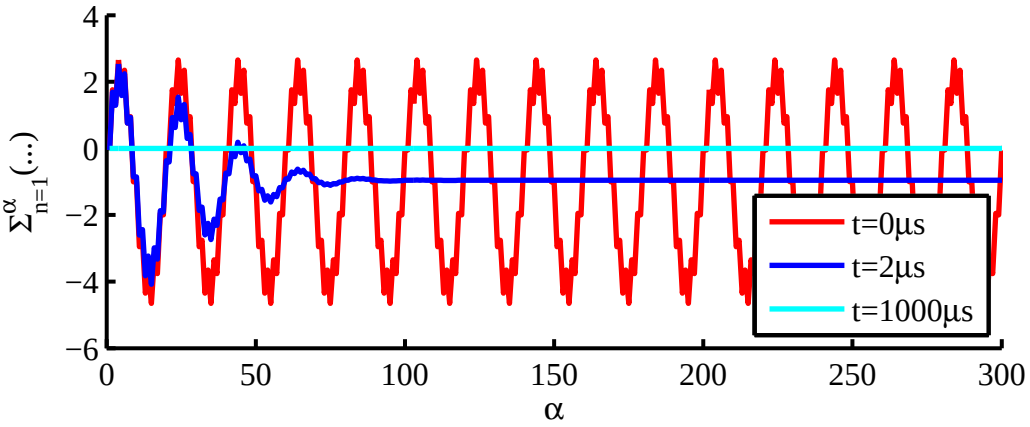

(b) Plot of Equation (3.2)

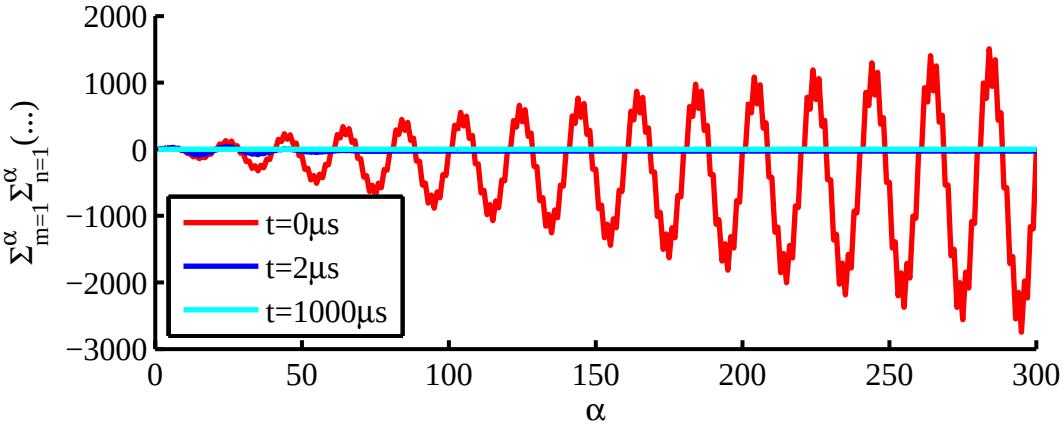

(c) Plot of Equation (3.3)

Figure 3.5: Convergence behavior of the analytical solution (Equation (2.4)).

the analytical solution needs to converge to avoid any ambiguity. This is achieved by neglecting the time between zero and two microseconds for both the FE simulation and the analytical solution. Then the analytical solution converges and a comparison is possible. Sufficient accuracy of the analytical solution in this research is defined for a value of $\alpha = 250$ as the upper limit for the summations.

3.3.2 Results of Convergence Test

Figure 3.6 illustrates the FE model used in the convergence test and shows the FE mesh as well as the source and the receiver position for the simulated ultrasonic measurement. The variation in the number of elements is conducted by modifying the number of nodes along the two sides of the uncracked model (illustrated in Figure 3.6). In Table 3.4 the investigated configurations with their respective number of elements along each side are given and the upper limit for the summations employed for the analytical solution, in accordance with the discussion of the previous section, are given. The parameter illustrated with d in Figure 3.6 refers to the distance between the symmetry line of the two-dimensional model and the source or receiver. This parameter is also varied in order to further analyze the convergence of the FE model towards the analytical solution. The values for d in the convergence test are chosen as $d = 30mm$ and $d = 60mm$.

After the simulation runs, in a similar fashion to the analytical solution, the FE simulation results need to be filtered in order to eliminate any effects at very low times,

Table 3.4: Test cases for convergence test.

Test case	1	2	3	4
Elements in x_1-direction	20	60	120	600
Elements in x_2-direction	10	25	50	250
Total number of elements	200	1500	6000	150000
n of eq. (2.4)	250	250	250	250
m of eq. (2.4)	250	250	250	250

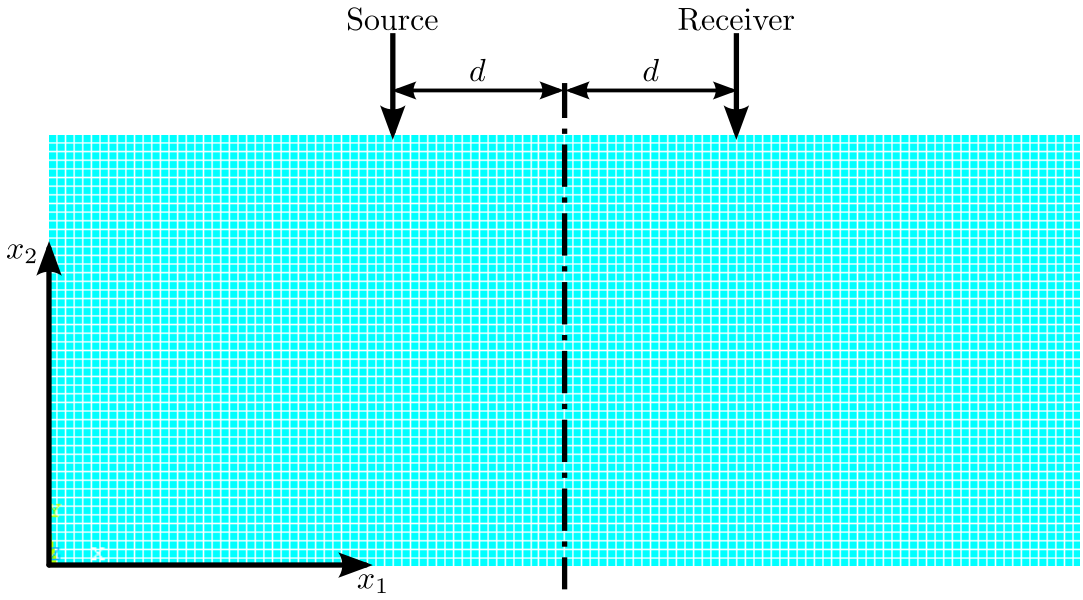

Figure 3.6: FE model of uncracked geometry with source and receiver.

which complicate the analysis unnecessarily. The impulse response of the uncracked FE model is illustrated in Figure 3.7 for the source receiver distance of $60mm$ (equals $2d$ in Figure 3.6). The impulse response describes the temporal behavior of the ultrasonic energy evolution in the material due to the excitation with a numerical impulse, as illustrated in Section 3.1.2. From Figure 3.7, it can be observed, that the maximum amplitude of the ultrasonic energy varies for the various number of elements regarded in the convergence test. This difference originates from the way Ansys treats heat generation defined on a node. In Ansys the nodal heat generation is split up into as many times as the number of adjacent elements, which contain the node that the heat generation is defined on. Moreover, the heat generation values are multiplied by the weighted area (volume for the three-dimensional case) of the elements which contain that node (weighted means the integral over the area, or volume, of the element of the product of the area or volume and the respective interpolation function). This leads to the fact that larger elements receive more heat generation than smaller elements and hence explains the different maximum

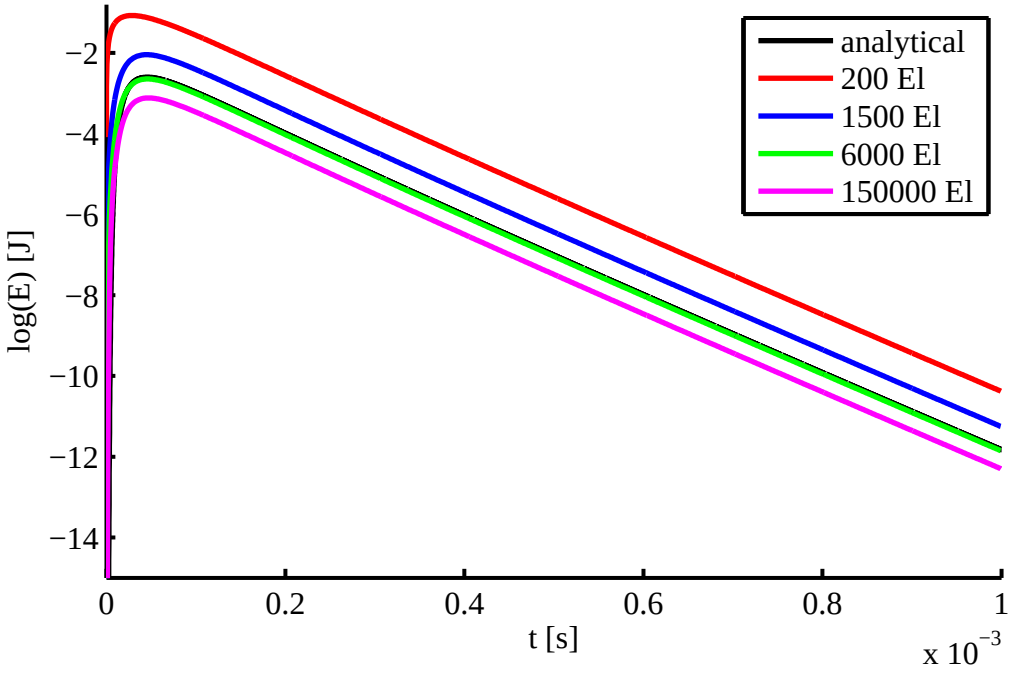

Figure 3.7: Energy-time curves for a source-receiver distance of 60mm to an impulse excitation.

amplitudes. The fact that the curve of the analytical solution and the curve of the FE simulation line up on top of each other is a coincidence. As a conclusion from this, the energy curves are normalized to magnitude one for an easier comparison without the loss of generality, as the maximum value is of no interest to the analysis.

The normalized impulse response energy curves of the uncracked FE simulation and the analytical solution are depicted in Figures 3.8a and 3.8b. From these figures, a first impression of the convergence can be obtained, which yields the conclusion that the FE simulation converges towards the analytical solution, implying the applicability of the FE model. This can be seen from the normalized curves lining up on top of each other for more than 200 elements. For a finer analysis of the convergence the two convergence criteria are validated.

The first is the peak energy arrival time error between the analytical solution and the various FE simulations with the peak energy arrival time t_{peak} being defined as the

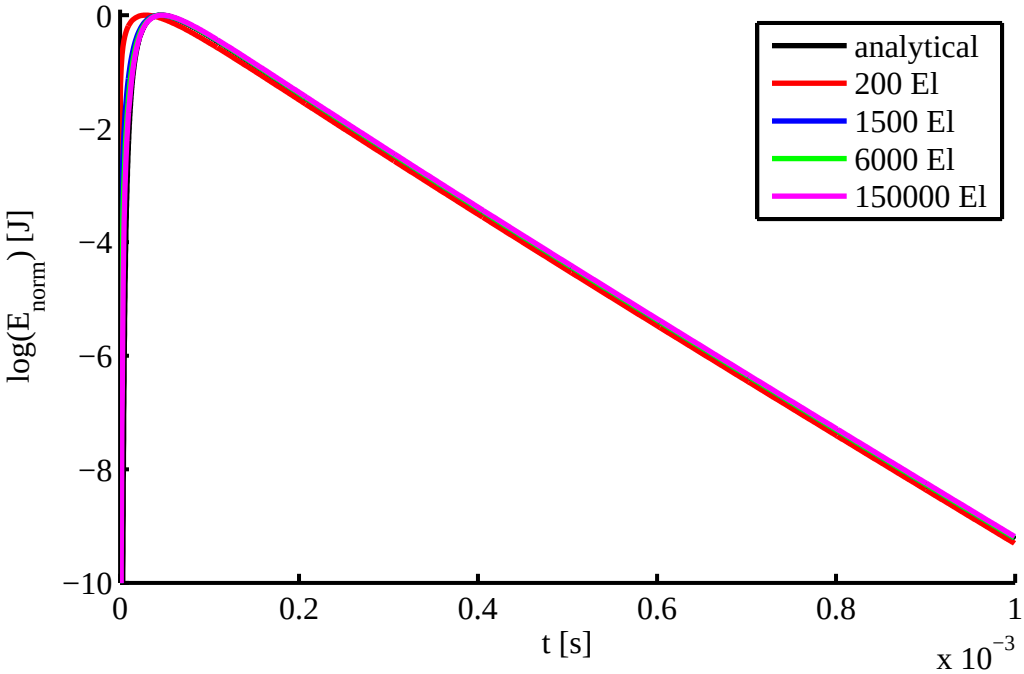

(a) Source-receiver distance of 60mm

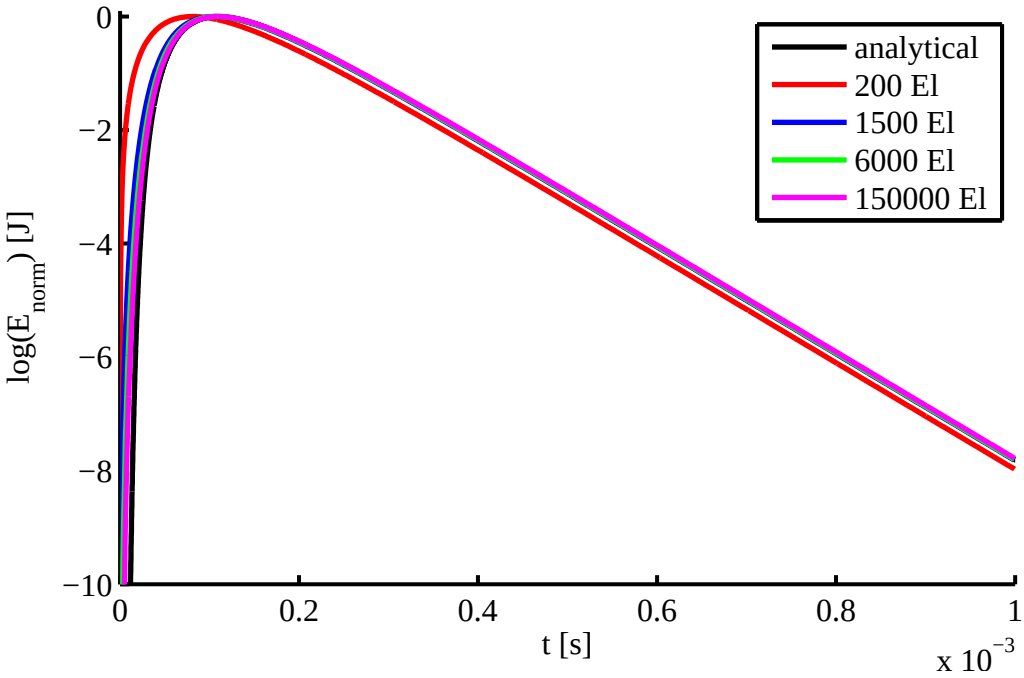

(b) Source-receiver distance of 120mm

Figure 3.8: Normalized energy-time curve of impulse response for convergence test.

maximum of the energy curve. This criterion is of relevance, as in the later analysis of various crack types the peak energy arrival time is used as the basic parameter for the crack depth determination. The criterion can be mathematically formulated as the relative error between the analytical solution and FE simulation and reads

$$rel.\ Error = \frac{t_{peak,analytical} - t_{peak,FEsim}}{t_{peak,analytical}} \cdot 100\%. \tag{3.4}$$

Equation (3.4) defines the relative error between the analytical solution and the FE simulations with respect to the analytical solution in terms of the peak energy arrival time. The relative error is then given in percent with 0% being the best. In Figure 3.9 the relative error for peak energy arrival time is illustrated for the various number of elements and the two source-receiver distances analyzed. It is observed that the relative error drastically decreases from 200 to 1500 elements for both source-receiver distances. In particular, the relative error for $60mm$ source-receiver distance drops from 38% to 1.5% and for the $120mm$ source-receiver distance from 25% to 3.7%. For an even larger number of elements the relative error is scarcely reduced for both source-receiver distances. Furthermore, for more than 6000 elements the relative error is below 2% which is considered an acceptable accuracy, considering that the increase to 150000 elements does not bring any significant improvement and only increases the computational effort tremendously.

The second convergence criterion considers the error of the energy curve between the analytical solution and the FE simulations. The idea is to quantify the error made by the FE simulation for the whole duration of the ultrasonic diffusion process, rather than just one point in time as with the peak energy arrival time. For this convergence criterion the normalized energy curves are regarded and this criterion can be mathematically described then as

$$\| \ error \ \|^2 = \| \ \mathbf{E}_{normalized,analytical} - \mathbf{E}_{normalized,FEsim} \ \|_2^2 \ . \tag{3.5}$$

In Equation (3.5) the variable $\mathbf{E}$ indicates the vector of all values of the ultrasonic

spectral energy density for every discrete point in time that is regarded. Further, Equation (3.5) resembles the square of the Euclidean norm defined on vectors. The evaluation of this convergence criterion is depicted in Figure 3.10. Similar to the peak energy arrival time convergence criterion, there is a large drop in the squared norm error from 200 to 1500 elements for both source-receiver distances. Moreover, the squared norm error remains on a constant level for the $60mm$ separation distance between the source and the receiver, whereas for the separation distance of $120mm$ the squared norm error decreases further for more than 1500 elements. Furthermore, as the squared norm error does not decrease majorly for more than 1500 elements, the usage of more elements only yields an increase in computational effort and not in accuracy. As a remark to this convergence criterion, it is to be mentioned that this criterion also tests the quality of the pre-filtering for both the analytical solution as well as the FE simulations, as otherwise the squared norm error would be very large.

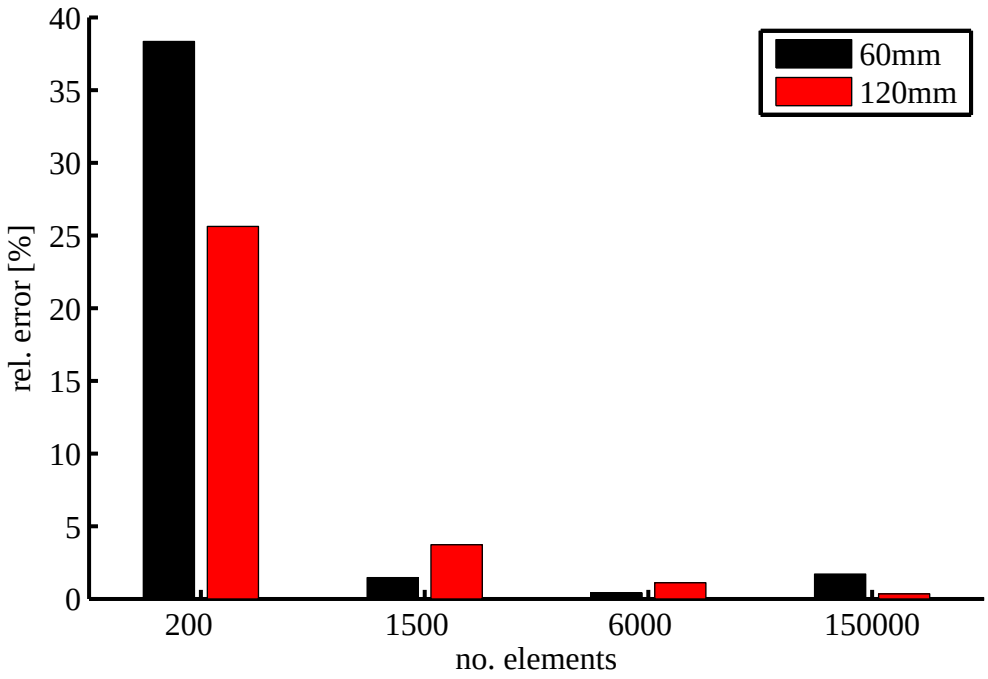

Figure 3.9: Relative error in peak energy arrival time of the FE simulations for two source-sensor distances.

To add to that, in this convergence criterion, the absolute values of the squared norm error are not meaningful and only the trend for an increasing number of elements should be considered.

3.3.3 Conclusions from the Convergence Test

The convergence test shows that the FE simulation converges well towards the analytical solution, implying the applicability of the simulation approach. Moreover, it can be concluded, that more than 6000 elements for a FE model yield good accuracy and will therefore be used as a reference value for the implementation of the cracked models.

3.4 Overview over the Various Cracked Models

In this section all the models for the various crack types regarded in this research are presented and specific modeling aspects are covered. Further, the parameters of each

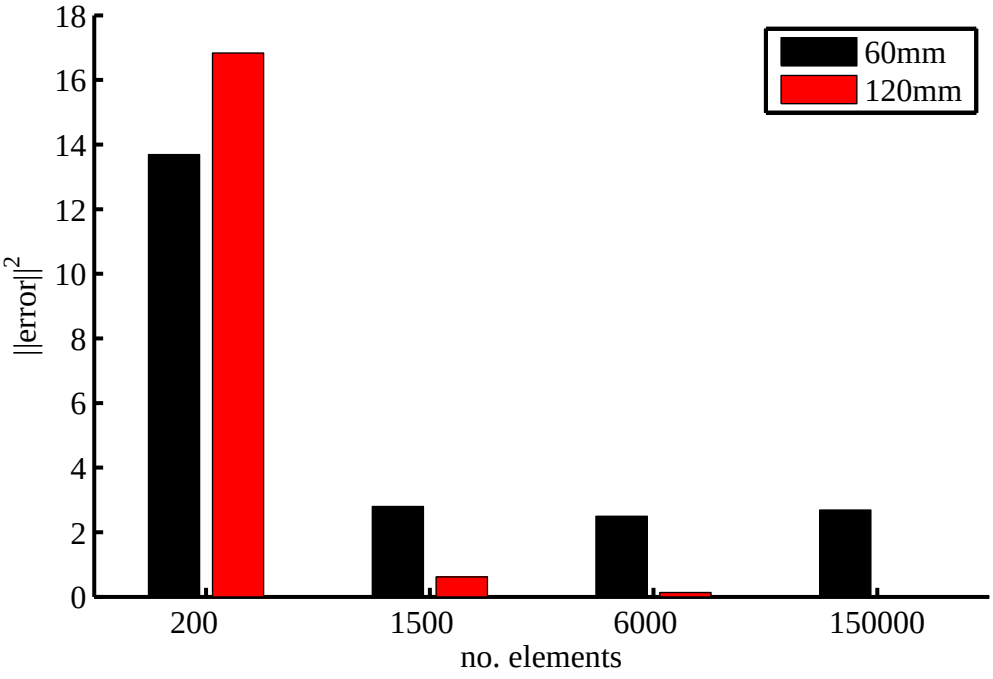

Figure 3.10: Square of the norm of the error between the normalized energy-time curves of the analytical and FE simulations for two source-sensor distances.

model are illustrated.

3.4.1 General Remarks on all Cracked Models

The cracked models are designed to be parametric, in order to facilitate generation and analysis of various test cases for the different crack types investigated. This means for example that the source-receiver distance can be easily modified. Moreover, the crack in all the models is presumed to be rectangular as Ansys does not tolerate the generation of several nodes at the same location. The width of the crack is chosen to be 1 mm. As the crack represents the feature of interest in the cracked models, special attention is give to the mesh generation around the crack and the crack tip. Around the crack tip, the FE mesh is refined with the goal of improving the spacial resolution in that region of the FE model. Due to the mesh refinement, the total number of elements increases compared to the uncracked model described in the convergence test. Furthermore, the cracked models are all based on the uncracked model, such that the lower limit for accuracy set by the convergence test is met. This means that all the cracked FE models contain more than 6000 elements.

3.4.2 Vertical Crack

Vertical cracks occur for example during a bending load and are generally due to excessive tensile stress. They are the simplest crack type and concrete specimen with this crack type can easily be cast as the crack geometry is not very complex. This fact also facilitates the modeling of vertical cracks. Moreover, the analysis goal of this crack type is to compare experimental ultrasonic measurements with the simulation results in order to give evidence to the finite element treatment of the diffusion approximation.

In Figure 3.11, as zoomed in view of the crack is shown, which is located along the vertical symmetry line of the FE model as illustrated in Figure 3.6. In Figure 3.11, also the parameters of the vertical crack type are illustrated, which are the

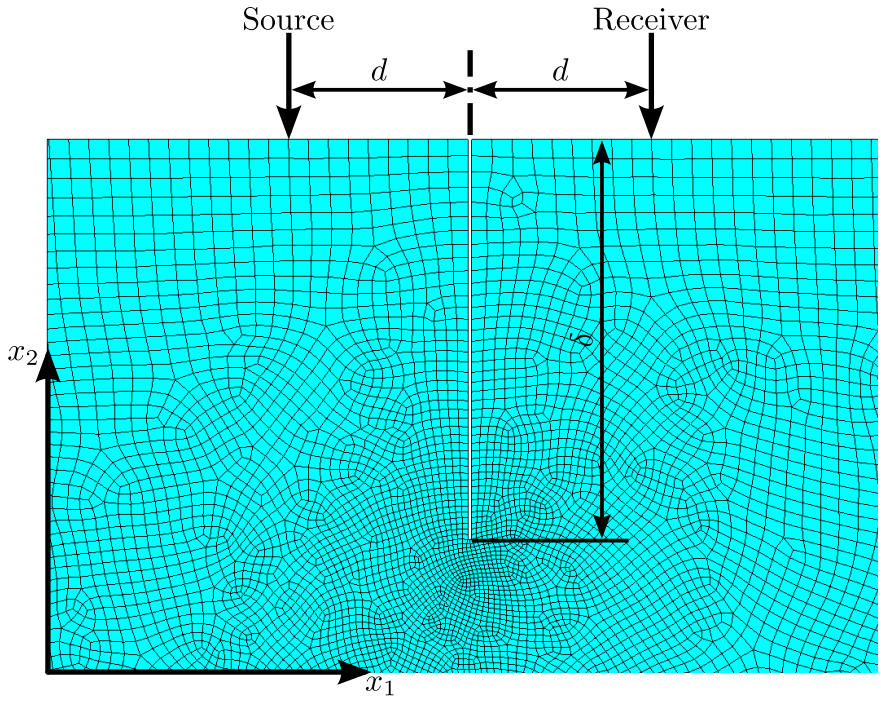

Figure 3.11: Zoomed in image of the FE mesh around the vertical crack with the parameters of the vertical crack type model.

crack depth δ and the source-receiver distance $2d$. Moreover, the mesh refinement around the crack tip can be seen as mentioned earlier in order to improve the spacial resolution. Furthermore, the coordinate frame depicted is only for reference and is actually located in the bottom left corner of the rectangular domain. The total number of elements in this model varies from 6000 to 9000 elements depending on the crack depth. The crack depth is varied from 0 mm to 125 mm which represents a crack depth of up to 50% of the height of the model and the source-receiver distance $2d$ is varied from 60 mm to 100 mm.

3.4.3 Reinforcement Bar Under Crack

With the goal to increase the tensile load resistance of concrete reinforcement bars, usually made of steel, are embedded in the concrete before the casting process. After subjected to bending loads a surface breaking crack may form near the reinforcement

bar. In field applications this crack type may promote corrosion of the steel reinforcement bar putting the structural integrity at risk. This crack type is therefore used to analyze the influence of a reinforcement bar under the crack tip on the ultrasonic measurements.

In Figure 3.12 the FE model of the crack type with a reinforcement bar under the crack is illustrated. The reinforcement bar is modeled as a circular shaped area, which has been cut out of the rectangular domain. The boundary conditions for the reinforcement bar are chosen as zero flux boundary conditions, arguing that the mechanical impedance mismatch of the concrete material and steel is large enough for that assumption. Moreover, the diameter of the reinforcement bar is 40 mm which corresponds to the diameter used in real concrete specimen. In the model, the center of the reinforcement bar is located 90 mm from the top surface. The diameter and the surface-to-reinforcement-bar-distance are obtained by measurement from an

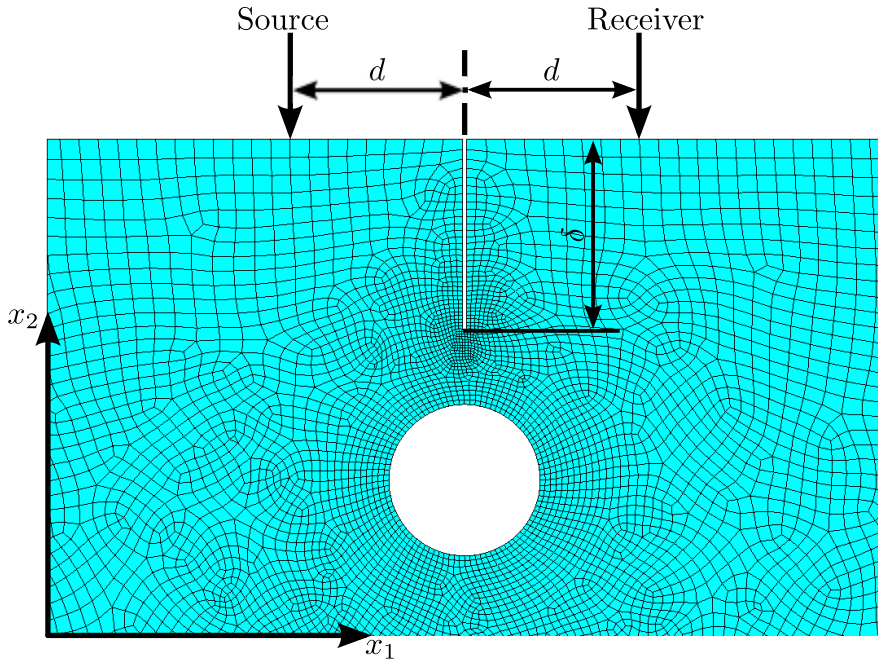

Figure 3.12: Zoomed in image of the FE mesh around the vertical crack with a reinforcement bar showing the parameters of the vertical crack with a reinforcement bar type model.

actual specimen. Furthermore, with the goal of improving the spacial resolution of around the reinforcement bar, the mesh density is increased around that location. The length of the crack above the reinforcement bar, which is denoted by the parameter δ, is varied from 0 mm to 50 mm and the source-receiver distance $2d$ from 60 mm to 100 mm. The FE model of this crack type contains approximately 10120 elements with slight variations due to different crack lengths.

As a general remark it is to be mentioned that this crack type is similar to the later introduced partially closed crack type with the hidden part having a circular shape rather than a rectangular shape. Moreover, the crack does not necessarily have to be vertical, but is modeled as such in order to make the model simpler.

3.4.4 Partially Closed Crack

This crack type occurs for example after a bending load, causing a vertical crack, is removed and the two faces of the crack are partially touching. The relevance of this crack type is given by the fact, that there is a hidden part of the crack that is not surface breaking and therefore would give insight into the possible limitations of the ultrasonic measurement technique.

In Figure 3.13 the FE model of this crack type is pictured. It can be observed that the partially closed crack model is a variation of the vertical crack type. It consists of a surface breaking part of the crack characterized by the parameter δ_1 and a hidden part of the crack. The length of the hidden part is determined by the parameters δ_2 and δ_3 which represent the starting and the ending depth of the hidden crack part, yielding the hidden length as their difference. For the simulation runs, the parameter δ_3 is maintained constant and the parameters δ_1, δ_2 are varied, which means that for a constant total crack depth the length of the hidden and surface breaking part of the crack are varied. Moreover, in case of this crack type, the source-receiver distance $2d$ is maintained at 60 mm. Furthermore, this model has approximately 8500 elements,

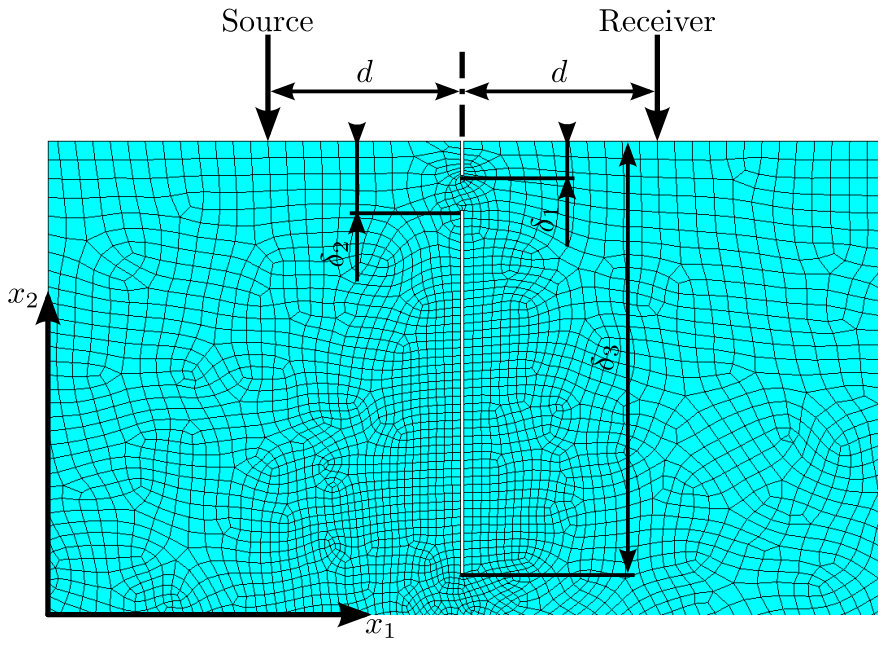

Figure 3.13: Zoomed in image of the FE mesh around the partially closed crack with the parameters of the partially closed crack type model.

which may vary slightly depending on the crack configuration.

As a remark to this crack type, it is to be mentioned that the general shape of the crack does not have to be vertical, but for the simplicity of modeling it has been assumed to be vertical.

3.4.5 Non-vertical Crack

Under a large bending moments on a concrete block, it can be observed that the crack geometry tends to kink away from a direction perpendicular to the surface. This can be explained by the different stresses acting in different depth in the material along the crack. The vertical part can be regarded as a crack due to tensile stress, whereas the non-vertical part is considered to be caused by shear stress. A photography of the non-vertical crack in Figure 3.14a has been taken of an actual concrete specimen under bending, which illustrates this cracking behavior and the vertical and non-vertical part can be clearly identified.

In Figure 3.14b the FE model used for this crack type is depicted. The vertical

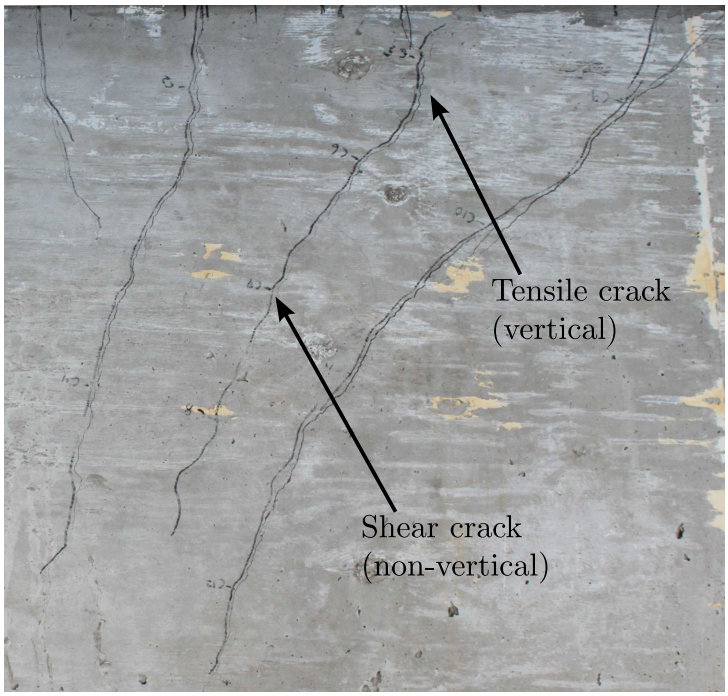

(a) Photography of a real crack on a bending specimen

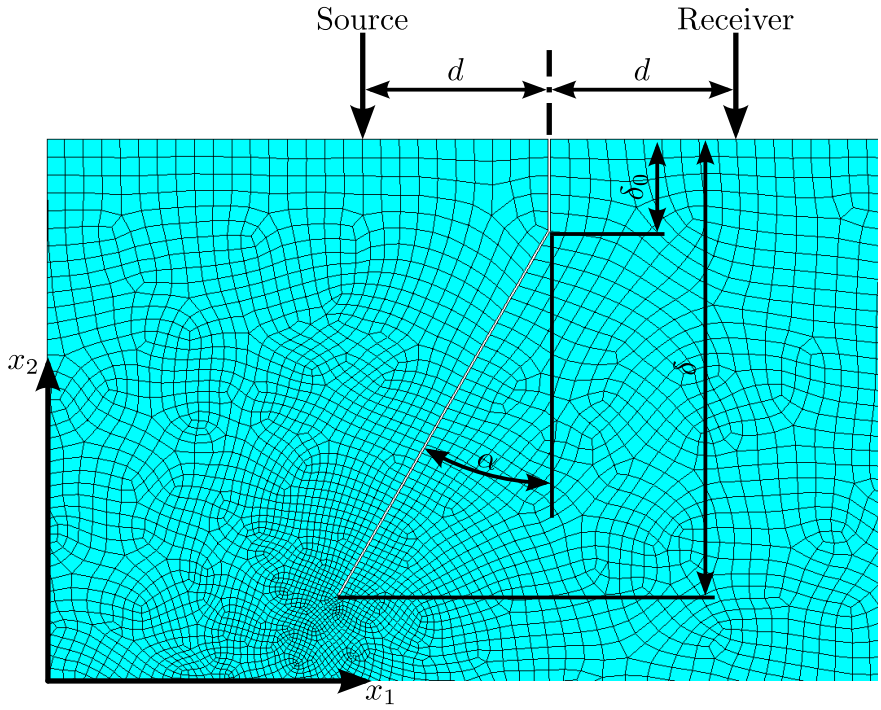

(b) FE model of the non-vertical crack with model parameters

Figure 3.14: Real crack and FE model of the non-vertical crack type.

part of the crack is located in the middle of the rectangular domain and is of the length δ_0. This length is kept constant throughout all the simulation runs of this crack type. The length of the non-vertical part of the crack is determined by the angle α and the projected crack depth δ and vertical crack depth δ_0. The angle α is systematically varied under consideration of different source-receiver distances $2d$ for all the simulation runs. Moreover, the number of elements of this model is approximately 8900. This number may vary for different crack configurations.

3.4.6 Two Parallel Vertical Cracks

Under a crack causing load, multiple cracks can occur as illustrated in Figure 3.14a with one possible scenario for this kind of crack type being a bending load. The FE model of this crack type is depicted in Figure 3.15 and has approximately 10600 elements, with the specific number depending on the length of the various cracks. The dash-dotted line in Figure 3.15 indicates a symmetry line which coincides with

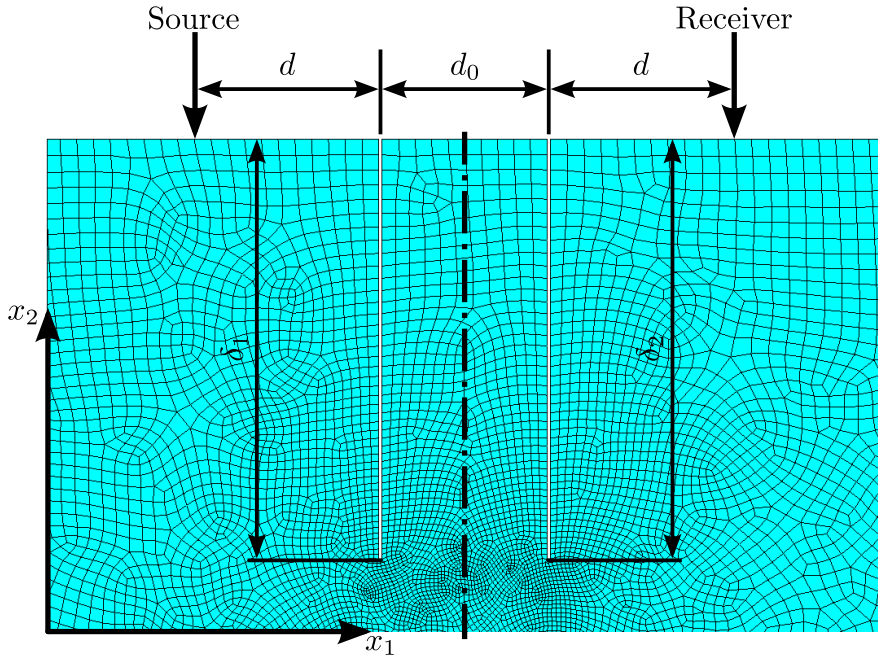

Figure 3.15: Zoomed in image of the FE mesh around two parallel, vertical cracks with the parameters of the two parallel, vertical crack model.

the symmetry line of Figure 3.6. Moreover, Figure 3.15 illustrates the parameters of this crack type model. The parameter d_0 refers to the separation distance between the two cracks and is chosen to be 50 mm. The length of both cracks is controlled by the parameters δ_1 and δ_2, which are varied between 40 mm and 100 mm. The sensor-crack distance d is given as 30 mm, yielding a total source-receiver distance of 110 mm, which is not varied during the simulation runs.

Finally it is to be noticed that both cracks do not necessarily have to be vertical or parallel.

CHAPTER IV

RESULTS

In this chapter, first, the simulation results of the vertical crack type are compared to experimental results and are analyzed. Then the simulation results of the other crack types are discussed.

4.1 Vertical Crack

In this section the vertical crack type is discussed starting with experimental evidence to the ultrasonic diffusion approximation and then analyzing the simulation results by itself.

4.1.1 Comparison with Experimental Results

As discussed in the last chapter, the FE model is based on an actual experimental setup with which ultrasonic measurements are taken. As a first step to validate the accuracy of the ultrasonic diffusion approximation, the experimental conditions are implemented in the FE model and the results are compared to the experimental measurements.

The parameters for the experimental validation are illustrated in Table 4.1 in accordance to the concrete specimens. The parameters δ and $2d$ of the vertical crack FE model are depicted in Figure 3.11. The value for $2d$ has been taken from [10] and it has proven to be a suitable value for ultrasound diffusion experiments based on experience. In Table 4.1 values for δ_{nom} and δ_{sim} are also listed. The reason for this is that the concrete specimens are cast to have the nominal crack depth δ_{nom} but after hand measurement with a thin plastic strip it is found that the crack depth is rather smaller. For the simulations therefore, the hand measured crack depth values

Table 4.1: Simulation configurations for the vertical crack type.

Configuration	1	2	3	4
D in $m^2 s^{-1}$	10	10	10	10
σ in s^{-1}	21000	21000	21000	21000
$2d$ in mm	60	60	60	60
δ_{nom} in mm	0.0	25.4	50.8	101.6
δ_{sim} in mm	0.0	22.0	45	92

δ_{sim} are used in order to model the actual specimen more accurately. Based on the data illustrated in Table 4.1 the FE simulations are conducted and the energy evolution curves of the experimental measurements, which have been obtained by In and presented in [10], and the FE simulations are depicted in Figures 4.1 and 4.2.

Figures 4.1 and 4.2 show the comparison of the impulse response of the experimental measurements and the FE simulations. The experimental energy evolution curves have been normalized because the spectral source energy density of the experiment is unknown. Out of that reason, the FE simulation energy evolution curves are scaled to best approximate the experimental data. This does not lead to any loss of information relevant to the analysis of the results. The treatment of the signal-to-noise ratio is therefore neglected as an absolute value for the signal amplitude would be required. Nevertheless, the noise level of the measurement can be identified in Figures 4.1 and 4.2 as the horizontal level of the signal fluctuation starting from about 0.5 ms to 0.7 ms. The beginning of the noise part also establishes the end of the signal which can be used for the comparison between simulation and experiment, as there is no noise in the simulation.

From Figures 4.1a, 4.1b and 4.2a it can be inferred that the ultrasound diffusion approximation is a valid assumption for concrete, as the energy curves of the FE simulation match with those of the experimental measurements. Only for the crack depth of 92 mm in Figure 4.2b, there is a slight difference between the experimental

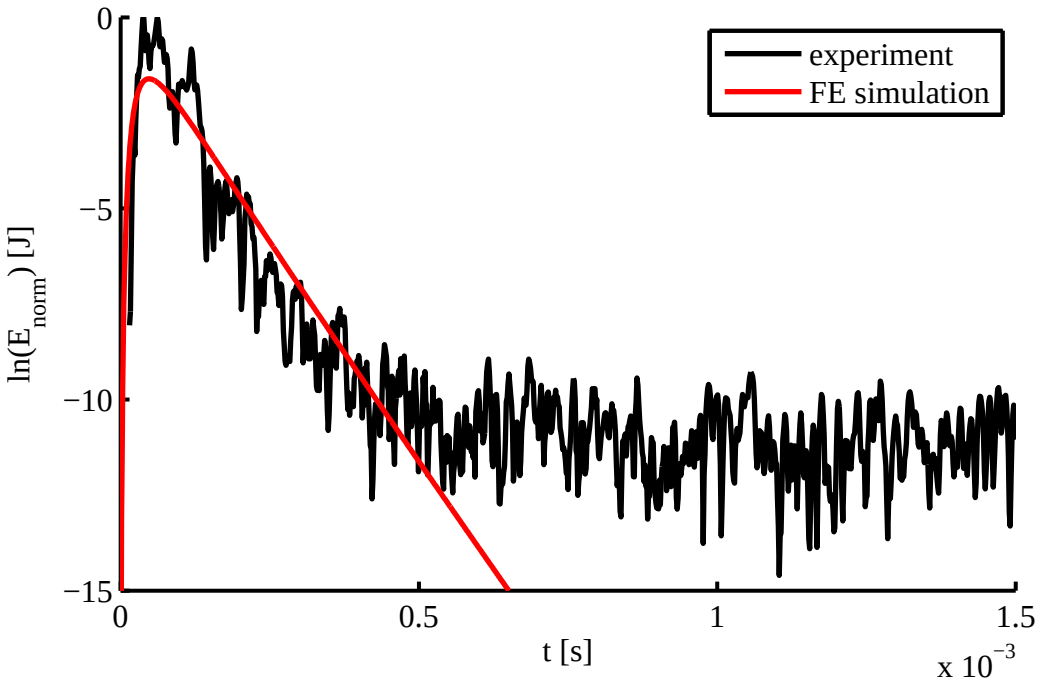

(a) No crack

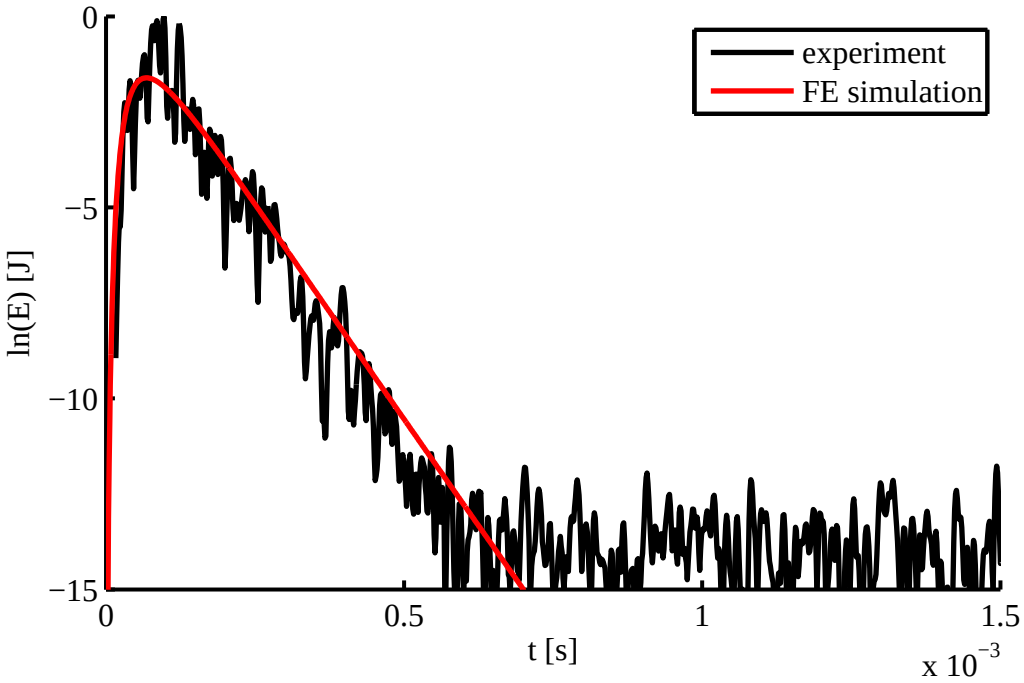

(b) 22 *mm* crack

Figure 4.1: Comparison between experiments and simulations for various vertical cracks part 1.

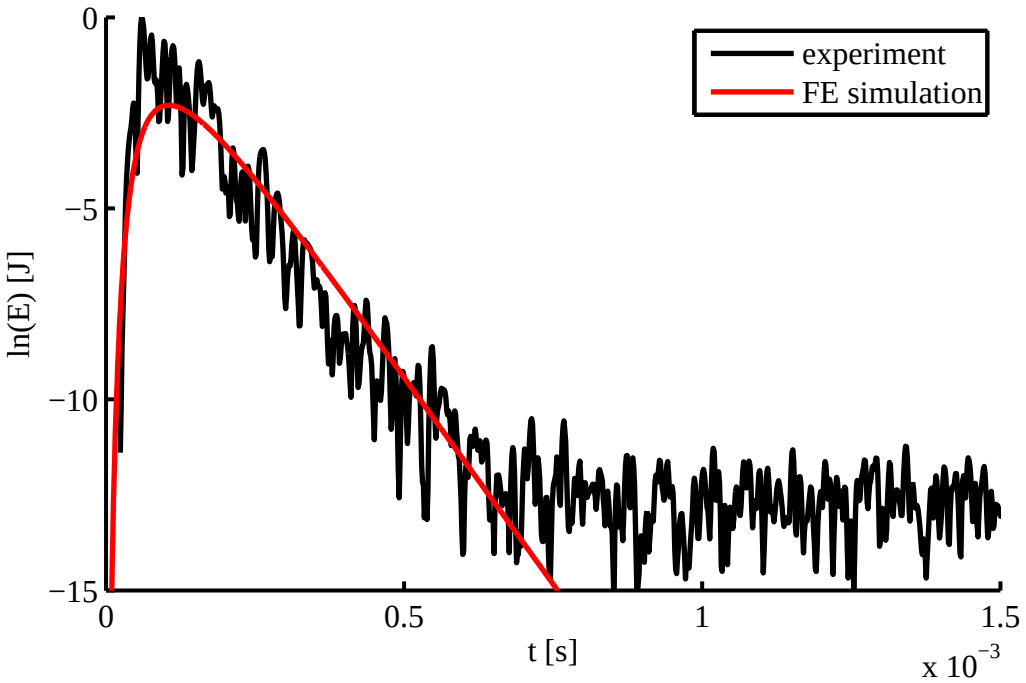

(a) 45 *mm* crack

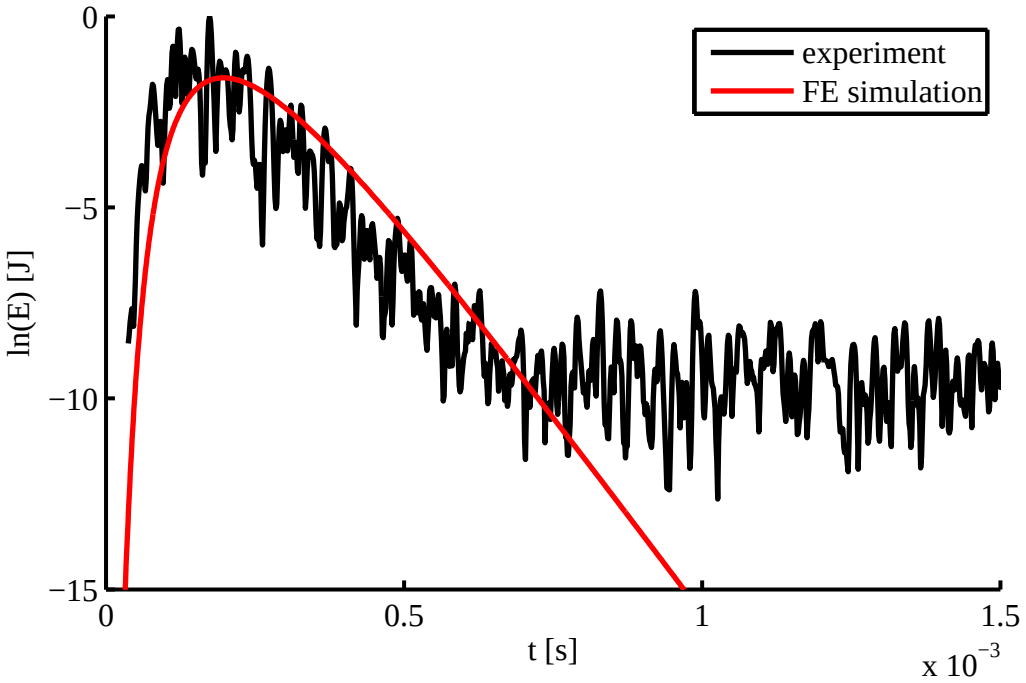

(b) 92 *mm* crack

Figure 4.2: Comparison between experiments and simulations for various vertical cracks part 2.

measurements and the simulation results, indicating that the crack depth is overestimated by the FE simulation. One cause for this mismatch could be that the real crack is shallower than determined by the hand measurement. It is also possible that the assumed diffusivity and dissipation coefficients are not accurate, such that errors are accumulated as the propagation distance is larger. Moreover, the experimental energy curves in Figures 4.1 and 4.2 show a fluctuating behavior, which can be explained by the finite number of scattering events happening in the specimen, as there are a finite number of scatterers embedded in the cement paste. The FE simulation on the other hand exhibits a smooth energy curve implying an infinite number of scattering events. The frequency used to recover the experimental energy curves is 500KHz. In general, the frequency is of no relevance to the FE simulations it only serves as a reference for a specific set of diffusivity and dissipation coefficients that are used to run the simulations.

As a conclusion form the comparison between the experimental measurements and the FE simulations it can be said that the there is a good agreement yielding the applicability of the ultrasound diffusion approximation. Moreover, this good agreement between experiment and simulations is used as a basis to justify the analysis of crack types other than a vertical crack.

4.1.2 Analysis of Simulation Results

In the section of the convergence test in the last chapter, the peak energy arrival time t_{peak} is used as a criterion for convergence. Moreover, the peak energy arrival time is used to compare different parameter configurations of the FE simulations. The parameters for this crack type are depicted in 3.11 and are chosen as following. The source receiver distance $2d$ is varied from 60 mm to 100 mm in steps of 10 mm. The crack depth δ is varied between 0 mm, 75 mm, 100 mm and 125 mm. After the simulation runs for all twenty possible permutations of $2d$ and δ, the maximum of the

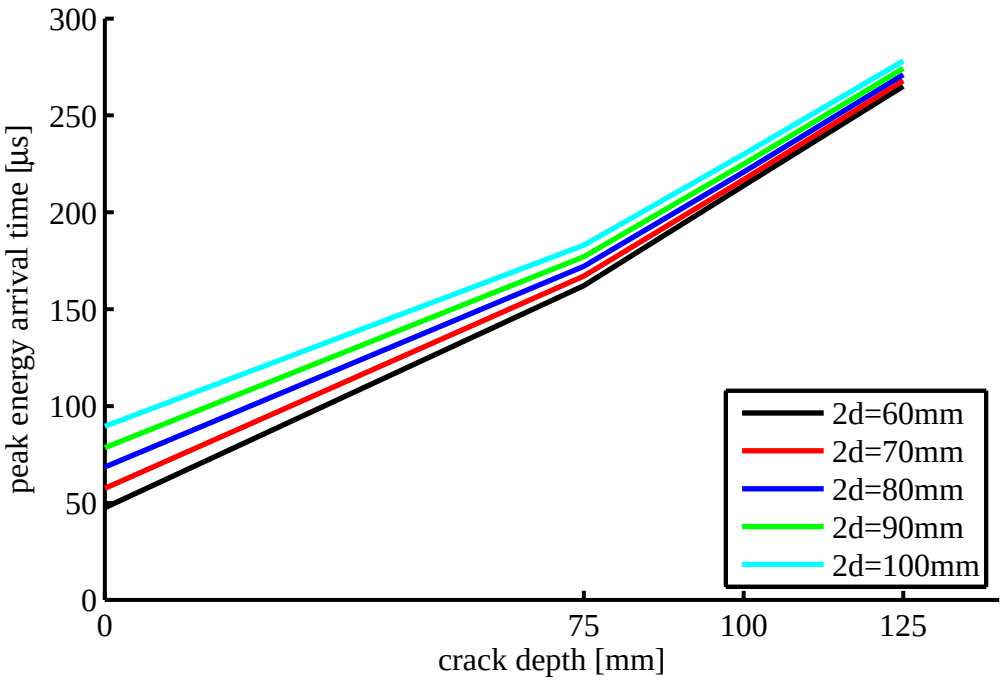

Figure 4.3: Peak energy arrival time for the vertical crack models regarding various source-receiver distances.

impulse response energy curve is determined, which is the peak energy arrival time.

Figure 4.3 illustrates the results of all the simulations for this crack type. It can be clearly seen, that with increasing crack depth, the peak energy arrival time also increases for all source-receiver distances. This behavior can be explained by the increasing propagation distance from the source to the crack tip to the receiver. Moreover, with increasing crack depth, the vertical distance between the curves decreases. This can be connected to the fact, that with a growing source-receiver distance, the influence of the crack depth on the minimum propagation distance decreases. The minimum propagation distance is the shortest path around the crack and in case of the vertical crack given by the distance between the source, the crack tip and the receiver. Furthermore, Figure 4.3 can be used to verify the plausibility of the FE simulation, which is given due to the above arguments.

In [14], a different approach is taken to evaluate the FE simulations of ultrasound

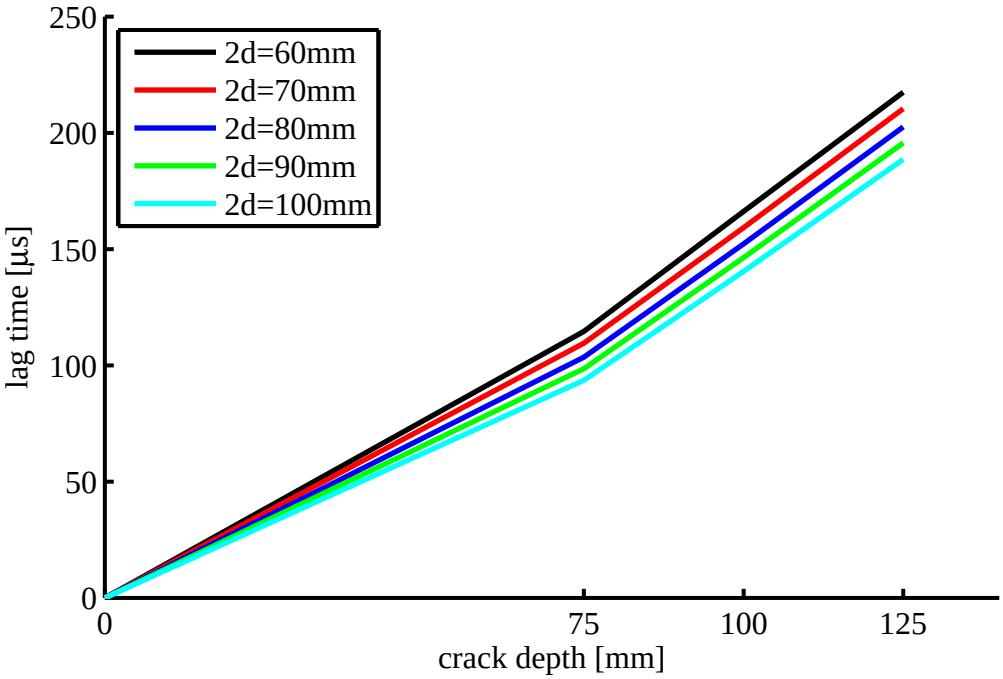

Figure 4.4: Lag time for the vertical crack models regarding various source-receiver distances.

diffusion. There, the lag time between the peak energy arrival time of the uncracked and the cracked simulations is regarded. The relationship between the lag time and the crack depth is depicted in Figure 4.4. There are two observations that can be made from this figure. Firstly, the lag time increases with increasing crack depth which is a logical consequence of the presence of the crack. Secondly, the increase in lag time is less for larger source receiver distances, which can again be explained with the minimum propagation distance and the same argument as before.

4.2 Reinforcement Bar Under Crack

For the simulation runs of the model with a reinforcement bar under the vertical crack, the parameters of Figure 3.12 have been chosen as depicted in Table 4.2. The source-receiver distance $2d$ is fixed to 60 mm and only the crack depth is varied. Moreover, the same configuration as illustrated in Table 4.2 is applied to the FE model with

Table 4.2: Simulation configurations for a reinforcement bar under the vertical crack.

Configuration	1	2	3	4	5
D in m^2s^{-1}	10	10	10	10	10
σ in s^{-1}	21000	21000	21000	21000	21000
$2d$ in mm	60	60	60	60	60
δ in mm	0	20	30	40	50

only the vertical crack (see Figure 3.11) in order to compare the two models and investigate the influence of the reinforcement bar under the crack. The normalized energy curves of the impulse response for all the simulations with and without a reinforcement bar are pictured in Figure 4.5. In Figure 4.5 the simulations with the reinforcement bars are illustrated as continuous lines, whereas the simulations with solely the vertical crack are drawn in dash-dotted lines. Also, the color references the

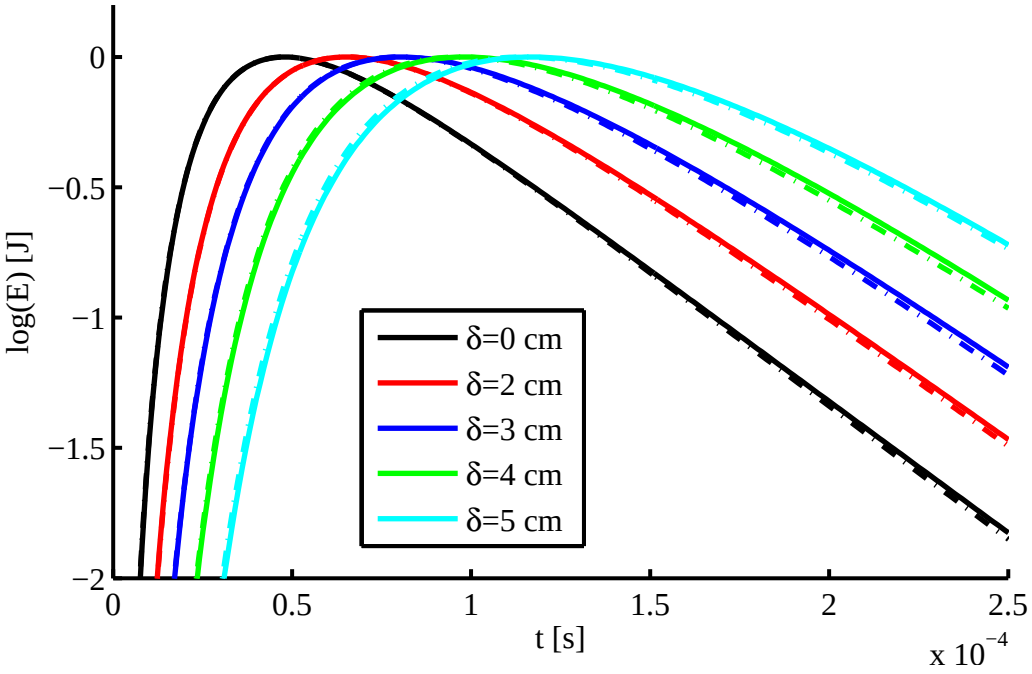

Figure 4.5: Comparison between the energy curves of the models with (full line) and without (dash-dotted line) for various crack depth δ (indicated by the color) with a source-receiver distance of $2d = 60\ mm$.

size of the vertical crack. From Figure 4.5 it can clearly be observed that the influence of the reinforcement bar is small. Furthermore, the influence of the reinforcement bar increases with increasing crack depth as the energy curves for both cases (with and without a reinforcement bar) do not match as well as for a smaller crack depth.

To further analyze the influence of the reinforcement bar, the peak energy arrival time for all energy curves of Figure 4.5 can be examined. In Figure 4.6 the peak energy arrival time is plotted over the crack depth for both models with and without the reinforcement bar. The color and line style scheme is the same as in Figure 4.5. From Figure 4.6 it can be seen that the peak energy arrival time of the cases with a reinforcement bar increases compared to the case without the reinforcement bar for larger crack depth. However, the deviation is very small as it is only of about $2\mu s$ indicating that the influence of the reinforcement bar is negligible and would not be

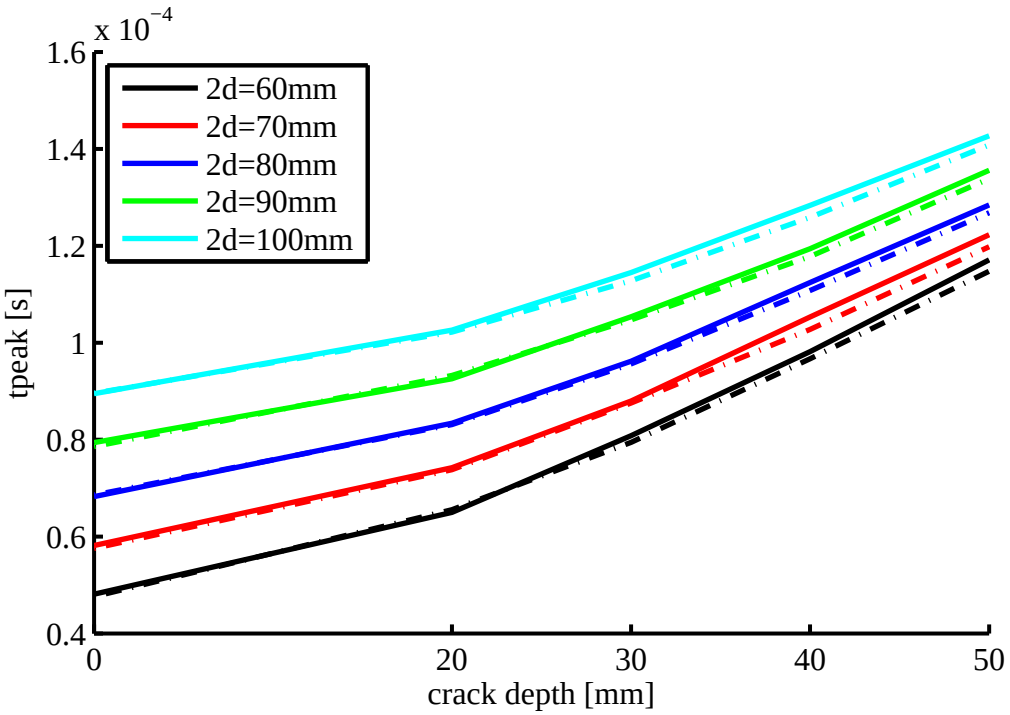

Figure 4.6: Peak energy arrival time for various simulation runs with (full line) and without (dash-dotted line) a reinforcement bar for different source-receiver distances $2d$ (indicated by the color).

of relevance to experimental measurements. Moreover, it can be expected that only a crack reaching the reinforcement bar would cause a significant change in the ultrasonic diffusion measurement, as in terms of a diffusion process, the ultrasonic energy would have to diffuse around the combination of the crack and the reinforcement bar itself yielding a different peak energy arrival time and energy curve and thus the reinforcement bar acts as an extended part of the crack.

In Figure 4.7 the evolution of the energy is depicted as a series of pictures taken from the FE simulation. The left three show the energy evolution with a reinforcement bar being present and the right three show the energy evolution without the reinforcement bar. The images are taken at the same times, $20\mu s$, $500\mu s$ and $1000\mu s$ in order to enable an adequate comparison. As explained in chapter two and three, that the FE simulation only delivers a dissipation free solution to the ultrasonic diffusion equation (2.1) and the dissipation term is accounted for after the simulation run by simple multiplication. This means that for the same point in time the spectral energy density values are scaled by the same factor and hence by neglecting a common factor no error is made. The numerical values underlying the contour colors are selected such that they are approximately the same for both images in order to attain a more accurate comparison. Further, the color red corresponds to a higher value, whereas the color blue to a lower value. The gradation from red to blue follows along the colors of the rainbow (rainbow spectrum). For this comparison of the energy evolution the maximum crack depth regarded in Table 4.2 is chosen as it exhibits the largest influence on the peak energy arrival time. Moreover, the goal of this figure is to give a qualitative impression of the difference in the ultrasonic energy diffusion process for both crack types. The comparison of Figure 4.7a and 4.7b reveals that there is no difference in both figures, as the diffusion process has not yet advanced to the location of the reinforcement bar. After $500\mu s$ the influence of the reinforcement bar becomes visible, as the energy is forced to diffuse around it. However, the shape

of the contours is not very different for Figures 4.7c and 4.7d, indicating the small influence on the ultrasonic diffusion process. Moreover, the major part of ultrasonic spectral energy density diffuses through the gap between the crack tip and the reinforcement bar, suggested by the contours. A similar impression is obtained from Figures 4.7e and 4.7f, in which the shape of the contour lines are only slightly different in the region of the reinforcement bar, but show the same behavior on the top surface of the model on which the sensor is located, as indicated by Figure 3.12. As a conclusion from Figure 4.7, it can be said that the FE images support the findings given by the analysis of the energy curves and peak energy arrival time, as Figure 4.7 also suggests the negligible influence of a reinforcement bar.

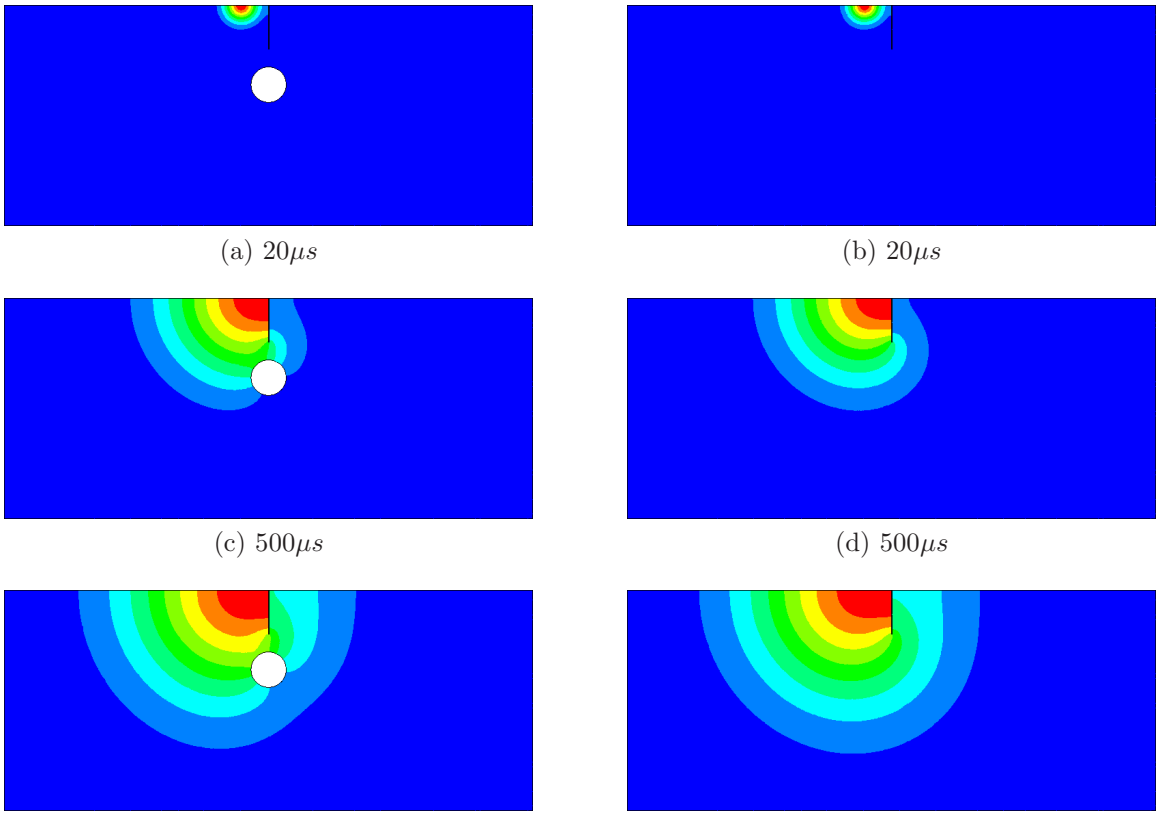

(a) $20\mu s$ (b) $20\mu s$

(c) $500\mu s$ (d) $500\mu s$

(e) $1000\mu s$ (f) $1000\mu s$

Figure 4.7: Comparison of the evolution of the ultrasonic spectral energy density without dissipation of the FE model with and without a reinforcement bar. The contours range from red being a high value to blue being a low value in a rainbow spectrum.

4.3 Partially Closed Crack

The simulations for this crack type are organized into three subsets characterized by a common maximum crack depth δ_3 as illustrated in Figure 3.13. The three maximum crack depths chosen in this analysis are 75 mm, 100 mm and 125 mm. In the following analysis, only the results of the 125 mm maximum crack depth are presented as the evaluation yields analogues results for the other two maximum crack depth subsets. The results for the other crack depth can be found in appendix A.

For each maximum crack depth, seven configurations are chosen to represent the various sizes of the surface-breaking and hidden part of the crack characterized by the parameters δ_1 and δ_2. The seven configurations for the maximum crack depth $\delta_3 = 125mm$ are listed in Table 4.3. From Table 4.3 it can also be seen that the source-receiver distance $2d$ is kept constant for all the simulation runs, as this is an established experimental value and the influence of this distance does not modify the general results strongly.

The simulation results of this crack type are compared to the simulation results of vertical cracks with a crack depth of δ_1 and δ_3 as it can be expected, that the peak energy arrival time for the partially close crack should lie between that of the vertical cracks used for the comparison. In Figure 4.8 this comparison is illustrated, with *pcc* being an abbreviation of partially closed crack. Further, *vcMin* represents

Table 4.3: Simulation configurations for partially closed crack type with a total crack depth of 125 mm.

Configuration	1	2	3	4	5	6	7
D in m^2s^{-1}	10	10	10	10	10	10	10
σ in s^{-1}	21000	21000	21000	21000	21000	21000	21000
$2d$ in mm	60	60	60	60	60	60	60
δ_1 in mm	10	30	50	60	70	80	90
δ_2 in mm	20	50	70	80	90	95	100
δ_3 in mm	125	125	125	125	125	125	125

the vertical crack simulation with a crack depth of δ_1 and *vcMax* the vertical crack with the crack depth of δ_3. From Figure 4.8 it can be concluded that the peak energy arrival time of the partially closed crack and the vertical crack with a crack depth of δ_1 are approximately the same. The difference between these two simulations is about $2\mu s$ which could comparable to numerical errors. This would imply that the ultrasonic energy mostly diffuses across the closed part of the crack leaving the hidden part undetected.

In order to determine what part of the fields energy diffuses across the closed part, the energy curves for configurations one and seven from Table 4.3 are compared to the respective simulations of the vertical crack with a crack depth of δ_1 and δ_3. Moreover, as the absolute value of the peak ultrasonic energy is of interest, the energy curves

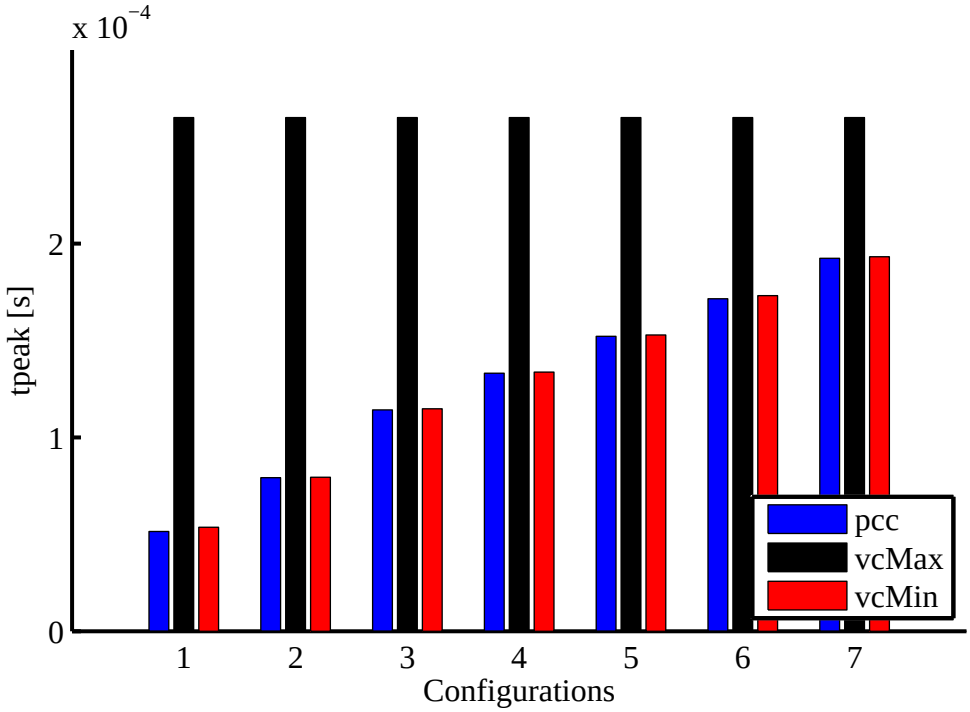

Figure 4.8: Peak energy arrival time for all the configurations of Table 4.3 of the partially closed crack type with a total crack depth $\delta_3 = 125mm$. In the legend *pcc* stands for partially closed crack and *vcMax* and *vcMin* represent the vertical crack with a depth of δ_3 and δ_1.

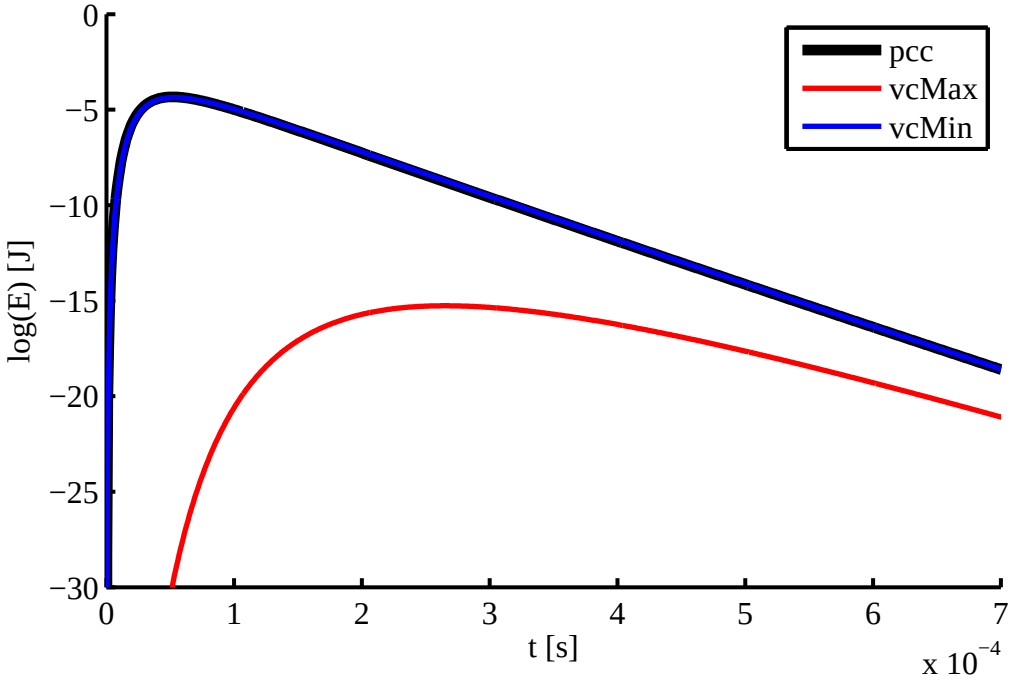

Figure 4.9: Comparison of the energy curves for configuration one in Table 4.3 with a vertical crack of a crack depth δ_1 and δ_3.

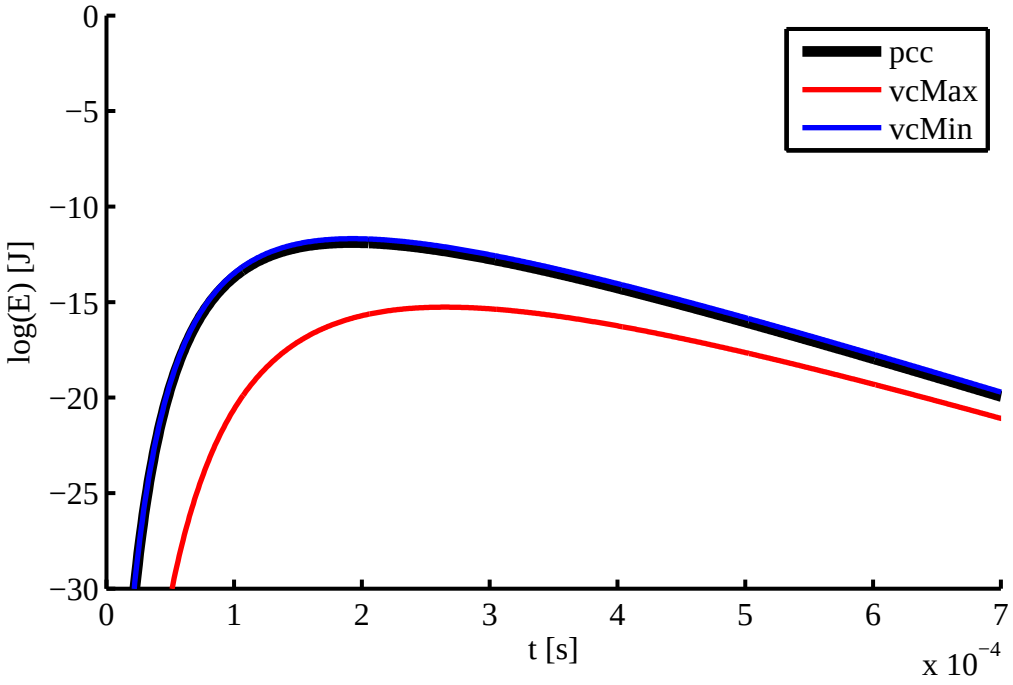

Figure 4.10: Comparison of the energy curves for configuration seven in Table 4.3 with a vertical crack of a crack depth δ_1 and δ_3.

are not normalized. The comparison between the three cases for configuration one is depicted in Figure 4.9. Configuration one represents the situation where the partial closure of the crack is located near the top surface of the model (see Figure 3.13), yielding a large hidden part of the crack. From Figure 4.9, it can be inferred that all the energy in case of the partially closed crack diffuses across the closed section of the crack as the energy curves for the partially closed crack and the vertical crack with crack depth δ_1 lie on top of each other. In Figure 4.10 this comparison is made for configuration seven from Table 4.3. This case is especially interesting, as the hidden part of the crack is very small and the ultrasonic energy could diffuse also around the hidden part. From Figure 4.10, although, it can be clearly seen that the energy curves for the partially closed crack and the vertical crack with the depth of δ_1 line up on top of each other, again implying that the ultrasonic energy preferably diffuses across the closed section of the crack.

In Figure 4.11 the evolution of the ultrasonic spectral energy density is depicted. The Figures 4.11a, 4.11c and 4.11e correspond to the simulation configuration one in Table 4.3 and Figures 4.11b, 4.11d and 4.11f represent simulation configuration seven in Table 4.3. Moreover, it has to be mentioned that the contour scaling differs for both configurations. Therefore, Figure 4.11 should be regarded as a qualitative illustration of the energy evolution than for direct comparison of the energy evolution around hidden cracks of different sizes. From Figure 4.11 it can then be inferred, that, as illustrated by the comparison of the energy curves in Figures 4.9 and 4.10, the ultrasonic spectral energy density preferably diffuses across the closed part of the the crack. In the case of configuration one, this behavior is exhibited stronger than in configuration seven, as the distance to the closed section of the crack is smaller than the distance around the hidden part.

As a conclusion from the simulation of the partially closed crack, it has to be noted, that the ultrasonic spectral energy preferably diffuses across the closed part

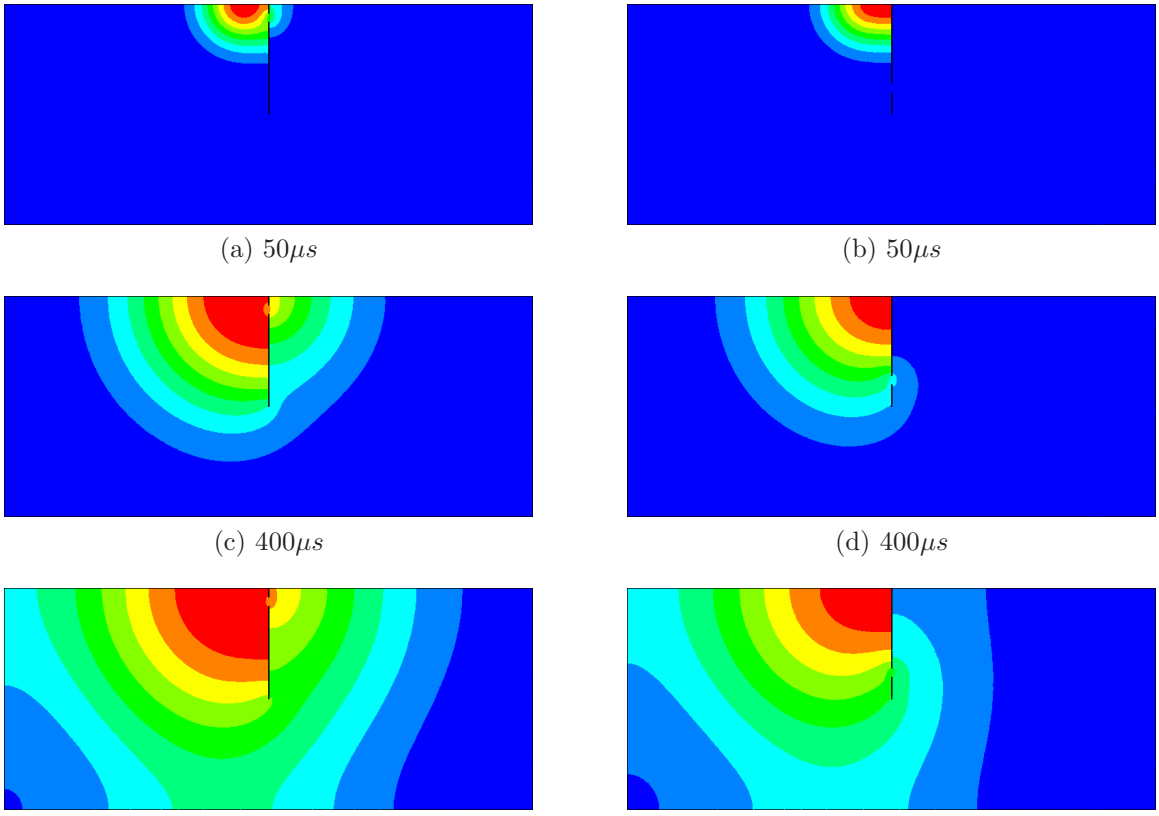

(a) 50μs (b) 50μs

(c) 400μs (d) 400μs

(e) 1000μs (f) 1000μs

Figure 4.11: Comparison of the evolution of the ultrasonic spectral energy density without dissipation of the FE model for configurations one (left) and seven (right) of Table 4.3. The contours range from red being a high value to blue being a low value in a rainbow spectrum.

of the crack, independent from the length of the surface-breaking or hidden part. This means that in the case of experimental measurements, the actual crack depth consisting of the surface-breaking and hidden part is underestimated by the extend of the hidden part. Moreover, the partially closed crack type simulations show one potential limit of the ultrasound diffusion technique for nondestructive evaluation of concrete, as the hidden part is not detected by the impulse response.

4.4 Non-vertical Crack

The parameters of the simulation model for the non-vertical crack type, according to Figure 3.14b, are depicted in Table 4.4. For a better comparison, the projected

Table 4.4: Simulation configurations of non-vertical crack type for all five source-receiver distances $2d$ analyzed.

Configuration	1	2	3	4	5	6	7
D in m^2s^{-1}	10	10	10	10	10	10	10
σ in s^{-1}	21000	21000	21000	21000	21000	21000	21000
δ_0 in mm	25	25	25	25	25	25	25
α in $^\circ$	-45	-30	-15	0	15	30	45
δ in mm	125	125	125	125	125	125	125

crack depth δ is maintained constant as with this crack type the influence of the angle is supposed to be analyzed. Moreover, the source-receiver distance $2d$ is varied from $60mm$ to $100mm$ in steps of $10mm$ for all the configurations listed in Table 4.4, yielding a total of thirty-five simulation runs for this crack type.

The peak energy arrival time for all the simulation runs is illustrated in Figure 4.12 as a function of the angle α. A negative angle indicates that the non-vertical part kinks to the left and a positive angle indicates kinking to the right, such that the angle is defined in a mathematically positive sense. From Figure 4.12 it can be seen, that the peak energy arrival time for the negative angles match approximately the values for the positive angles. The differences in the peak energy arrival time could be due to numerical errors. This implies that the simulated measurement fails to identify the kinking direction of the non-vertical part of the whole crack. In order to analyze this behavior further, the energy curves for all configurations in Table 4.4 with a source-receiver distance $2d$ of $60mm$ are compared and in appendix B for the remaining source-receiver distances. This comparison is shown in Figure 4.13. From Figure 4.13 it can be seen that the impulse response energy curves line up on top of each other when comparing a positive with the respective negative angle. The matching of the energy curves suggests that the impulse response for both kinking directions are the same, which means that there is an ambiguity and the kinking direction is not uniquely determined. Moreover, it can be observed from both Figure

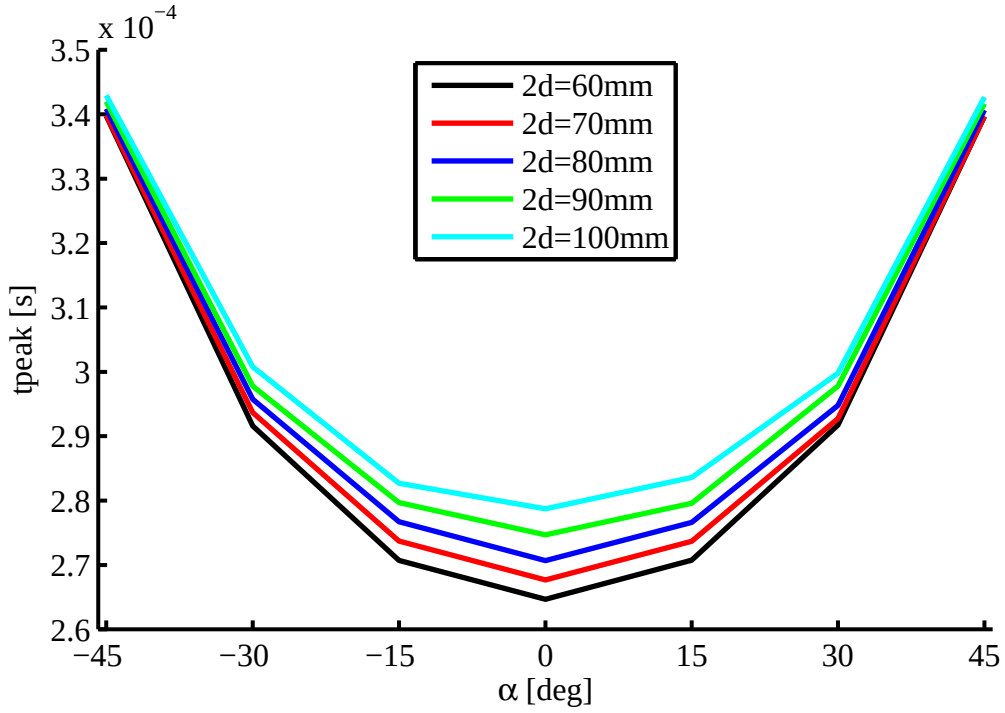

Figure 4.12: Peak energy arrival time for non-vertical crack type simulations in dependence of the angle α.

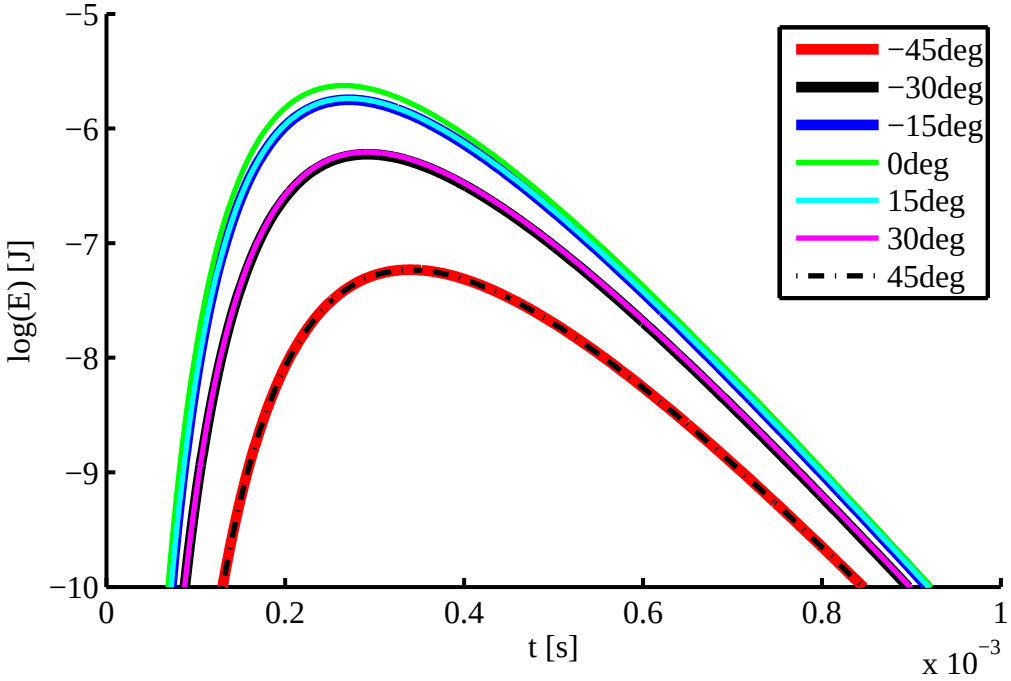

Figure 4.13: Comparison of the energy curves for the non-vertical crack crack type at a source-receiver distance of $2d = 60mm$ in dependence of the angle α.

4.12 and 4.13 that the peak energy arrival time increases for increasing angles, as the shortest distance between the source and the receiver increases. This yields a plausibility check for the simulation results.

As a conclusion from the simulation of the non-vertical crack, it can be said that the kinking direction is not uniquely determined by a diffuse ultrasonic technique and further knowledge of the potential kinking direction is required.

4.5 Two Parallel Cracks

This test case is used to analyze the influence of multiple cracks on the impulse response for the spectral energy density. The simulation parameters used in the analysis are listed in Table 4.5 and correspond to the parameters illustrated in Figure 3.15. In order to eliminate the influence of other parameters, the crack separation distance d_0 and the source-receiver distance are maintained at constant values, as only the influence of the two vertical cracks is of interest and are systematically varied.

The evaluation of the simulation results is achieved by comparing the peak energy arrival time for the various cases. This comparison is pictured in Figure 4.14. From Figure 4.14, it can be inferred that the depth of the cracks given by δ_1 and δ_2 yields approximately the same peak energy arrival time. This can be seen by comparing configurations one with two and three with four. Moreover, to evaluate the plausibility of the simulation results, in configurations five, six and seven of Table 4.5 the crack

Table 4.5: Simulation configurations for two parallel vertical cracks.

Configuration	1	2	3	4	5	6	7
D in m^2s^{-1}	10	10	10	10	10	10	10
σ in s^{-1}	21000	21000	21000	21000	21000	21000	21000
$2d$ in mm	60	60	60	60	60	60	60
d_0 in mm	50	50	50	50	50	50	50
δ_1 in mm	50	40	50	60	25	50	100
δ_2 in mm	40	50	60	50	25	50	100

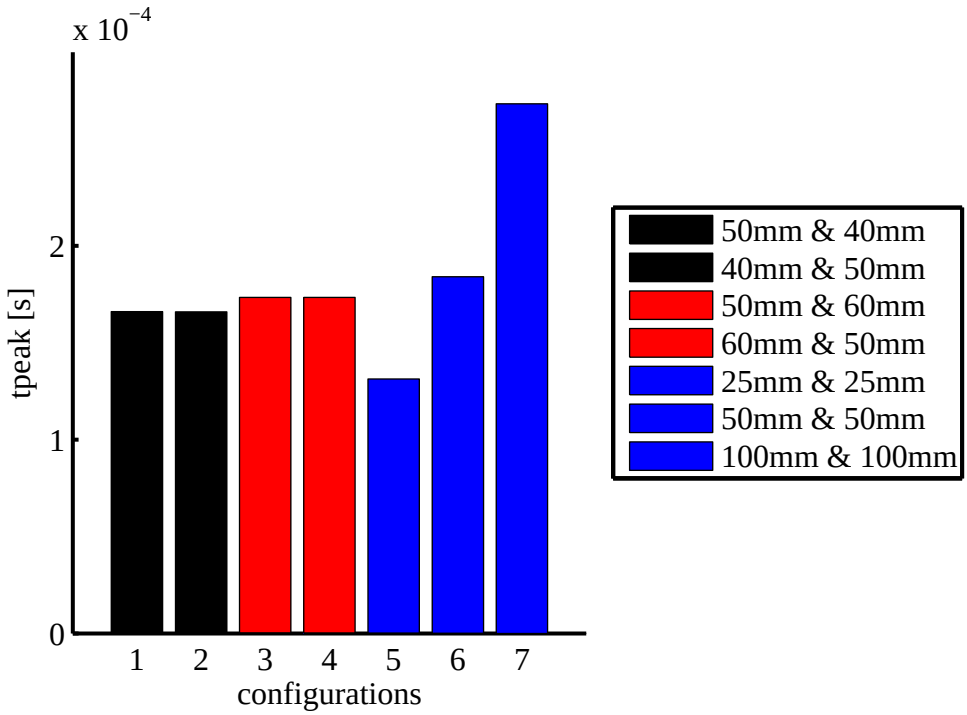

Figure 4.14: Comparison of the peak energy arrival time for the double parallel crack type for various crack configurations of Table 4.5.

depth of both cracks is set to equal values and only the depth is varied. As Figure 4.14 shows, the peak energy arrival time increases with an increase in the crack depths, demonstrating the plausibility of the simulation results.

With the peak energy arrival time being approximately the same for the configurations one and two as well as three and four, the energy curves of the impulse response are considered, as the peak energy arrival time is not a unique criterion to characterize the crack. The impulse responses for the configurations of Table 4.5 are depicted in Figure 4.15. The comparison of configurations one (black bar) and two (magenta bar) illustrates a good match of the impulse responses. A less accurate match is achieved by configurations three (blue bar) and four (red bar), where there is a slight amplitude mismatch. Moreover, the green line represents configuration five of Table 4.5 and is used as a reference impulse response in such a sense that curves with a shorter minimum propagation distance between source and receiver around

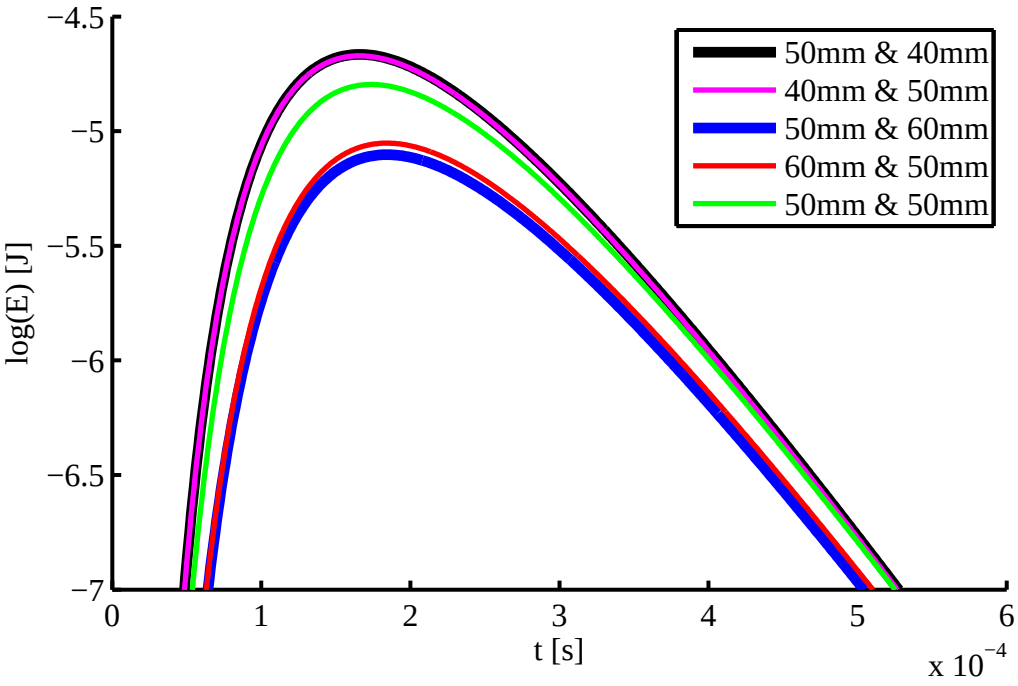

Figure 4.15: Comparison of the energy curves or the double parallel crack type for various crack configurations of Table 4.5.

the two cracks should have a higher amplitude, whereas longer minimum propagation distances should show lower amplitudes. In the case of these simulations this check for validity is satisfied.

In conclusion, the impulse response for two parallel cracks does not differ from that of a single crack, as the impulse responses of for example for the non-vertical crack type in Figure 4.13 does not differ from Figure 4.15. This indicates that ultrasonic measurements cannot resolve multiple cracks and for experimental analysis this needs to be considered. Therefore, cracks should be investigated separately, if separate sizing of each crack is desired. Moreover, as under permutation of the crack depth, the same impulse response is obtained, yielding that the diffuse ultrasonic simulations simply determine the minimum propagation distance through the material. Furthermore, this crack type represents another limitation to the diffuse ultrasonic technique.

4.6 Comparison of all Crack Types

The previous analysis of the various crack types has shown that there are some ambiguities regarding the identification of for example the size, the kinking direction or even the number of cracks between the source and the receiver. In addition, a common observation is that the diffuse ultrasound simulations always determine the shortest path between the source and the receiver through the material (minimum propagation distance). Therefore, for all the simulations considered in this research the peak energy arrival time is plotted against the minimum propagation distance in Figure 4.16. From Figure 4.16, a linear relationship between the peak energy arrival time and the minimum propagation distance is observed, as with an increasing peak energy arrival time, the minimum propagation distance also increases. Moreover,

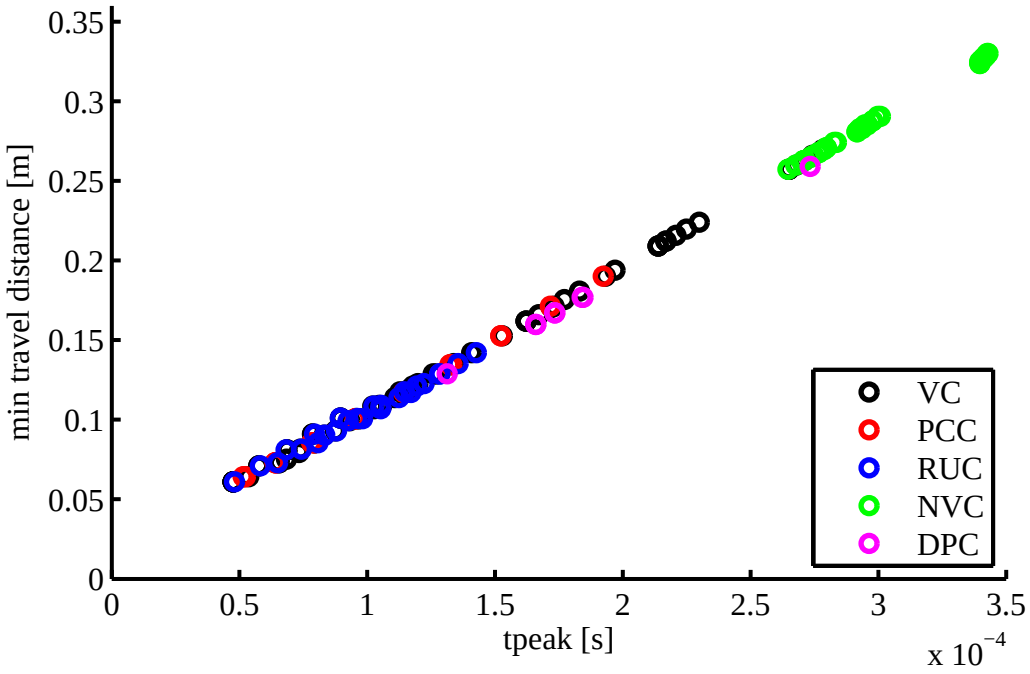

Figure 4.16: Minimum propagation distance between source and receiver via the crack tip versus the peak energy arrival time for all conducted simulations in this research. In the legend, *VC* refers to vertical crack, *PCC* to partially closed crack, *RUC* to reinforcement bar under crack, *NVC* to non-vertical crack and *DPC* to double parallel crack.

because all the simulation results show a linear behavior in terms of the minimum propagation distance and the peak energy arrival time and the previous findings, it can be concluded that the peak energy arrival time is independent of the shape of the crack. Furthermore, this implies, that an arbitrarily shaped crack or system of cracks would yield the peak energy arrival time of the minimum propagation distance between source and receiver and therefore preliminary knowledge of the cracking geometry is required to correctly interpret the measurements.

One limitation of the relationship depicted in Figure 4.16 is that it is restricted to one combination of diffusivity and dissipation coefficients or one frequency. For field applications and laboratory experiments this means that the diffusivity and dissipation coefficients must be determined right before the measurement on a crack, as other forms of damage might alter the initial scattering coefficients right after casting. In for example [8], the influence of heat and ASR damage on the diffusivity and dissipation coefficients are evaluated as a function of time and are found to generally decrease with the damage state, implying the a priori determination as mentioned earlier.

In Figure 4.17 the minimum propagation distance versus peak energy arrival time is fitted with two different linear functions. The first is a straight line starting from the origin of the coordinate system, $y = mx$, as it is expected that for a peak energy arrival time of zero, the minimum propagation distance should be zero too. However, a fit with a linear function with a constant term of the form $y = mx + c$ exhibits a better approximation of the simulation results. In Table 4.6 the recovered coefficients for both fits are listed. The slope of the line can be understood as a kind of average speed, with which the maximum energy propagates. Furthermore, it is expected that the slope shows some correlation with the diffusivity and dissipation coefficients, as in [14], where the influence of dissipation and diffusivity has been investigated and it was found that higher values for diffusivity and dissipation reduce the peak energy

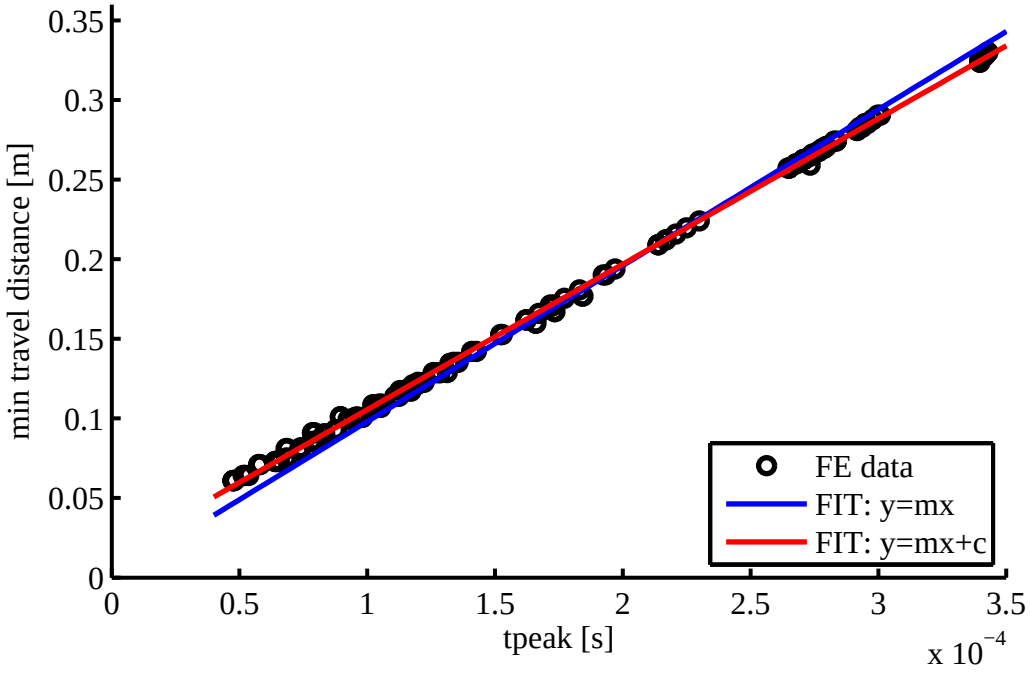

Figure 4.17: Minimum propagation distance between source and receiver via the crack tip versus the peak energy arrival time for all conducted simulations in this research, fitted with two linear functions.

arrival time.

4.7 3D FE Model

The three-dimensional model is also derived from the actual concrete specimen, which illustrated in Figure 3.1. The motivation of the three-dimensional model is that the position of the source and receiver relative to the crack is not necessarily in the crack's symmetry plane. This is of particular interest, as due to the previous results of this research, the diffuse ultrasonic technique supplies the impulse response for the shortest

Table 4.6: Coefficients for linear fits.

	m in ms^{-1}	c in m
$y = mx$	980.1	0.0
$y = mx + c$	914.1	0.01412

distance between source and receiver and would yield a possible underestimation of the actual crack. Moreover, a three-dimensional model would offer simulating a broad variety of other cracks that could only be considered with a three-dimensional model.

The geometry of the three-dimensional model is defined, in accordance to the real concrete specimen, with $600mm \times 250mm \times 300mm$ as length×height×depth. The excitation of the three-dimensional model is according to the two-dimensional model and located on the symmetry plane around the depth dimension. The diffusivity and dissipation coefficients are taken from the 2D simulations. The goal of the three-dimensional simulation is to explore the possibilities of simulation in three dimensions and in this research only a uncracked simulation is presented. The reason for this is that the solving of a cracked 3D model is not possible, as the available Ansys license restricts the total number of elements.

In Figure 4.18 the ultrasonic energy evolution without dissipation is illustrated for the 3D model. From Figures 4.18a and 4.18b, the spherical diffusion of the ultrasonic energy can be clearly seen, until the diffusion process reaches the boundaries and in Figure 4.18c the case of an almost plane-like diffusion pattern can be observed. Moreover, Figure 4.18 illustrates that the assumption of a two-dimensional model is actually wrong as there is no plane-like diffusion pattern in the experimental measurements. The two-dimensional model still retains its validity, as the diffusion and dissipation coefficient are recovered using a two-dimensional model and are lower than a recovered coefficient set with a three-dimensional model. This means that the 2D model accounts for the three-dimensional diffusion behavior with lower coefficients. A comparison of two- and three-dimensional recovery methods for the diffusivity and dissipation coefficient can be found in [8], where the recovered coefficients for a 3D model are found to be higher than for a 2D model.

As a conclusion from the 3D model, it can be noted that the simulation in 3D is possible and that this will open a broad spectrum of possible simulation configurations

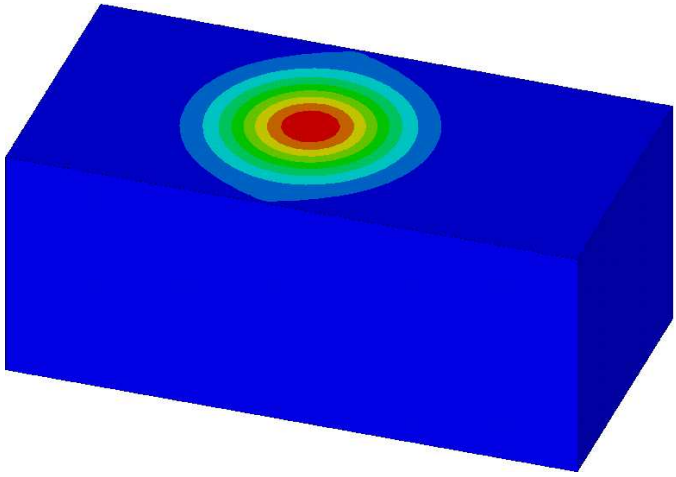

(a) 195μs

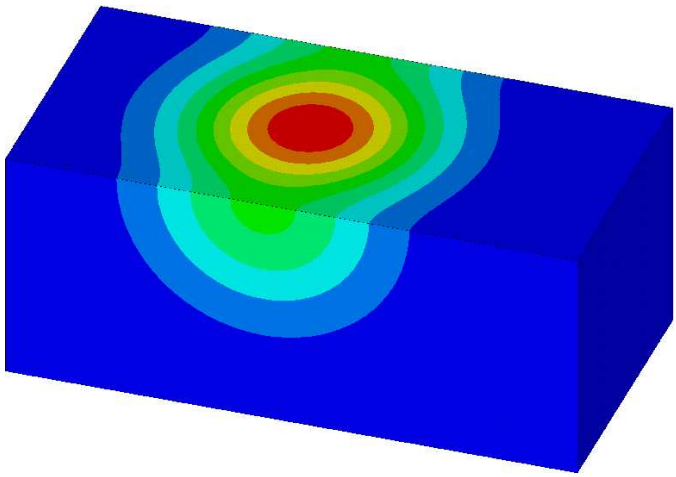

(b) 400μs

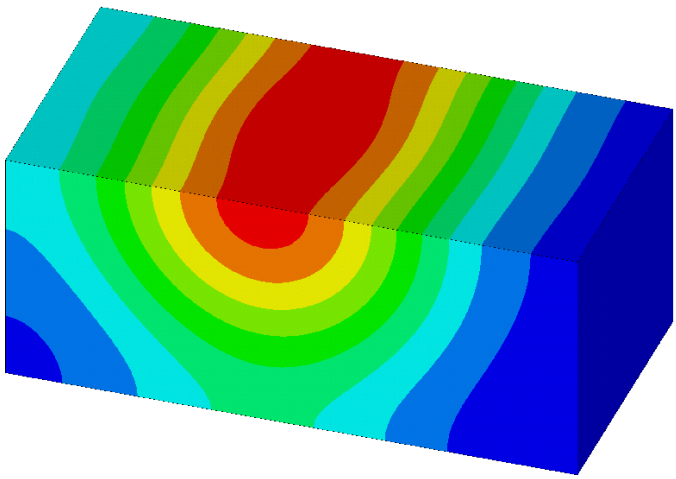

(c) 1000μs

Figure 4.18: Evolution of the spectral energy density without dissipation in the 3D model.

for future work. Moreover, it is to be mentioned that a three-dimensional simulation requires scattering parameters which are recovered using a three-dimensional analytical model in order to accurately model the experimental setup.

CHAPTER V

CONCLUSION AND OUTLOOK

In this research the finite element method was used to simulate experimental measurements of ultrasound diffusion in concrete. A two-dimensional FE model was implemented for the experimental setup and the convergence of the FE model with an analytical solution was validated. Moreover, the simulation results were compared to experimental measurements showing a good agreement between the simulation and experiments. Based on the agreement between experiment and simulation, various other crack types were analyzed.

The results of the finite element simulations showed that there are certain limitations for measurements with diffuse ultrasound. It was shown that the impulse response of a partially closed crack resembles the response of a vertical crack of only the surface-breaking part of the partially closed crack. Moreover, it was found that the kinking direction of a non-vertical crack cannot be determined from the impulse response. Furthermore, the impulse response for two cracks implied that it is not possible to individually detect the cracks from the diffuse ultrasonic response. In addition, the presence of a reinforcement bar under the crack tip does not greatly influence the impulse response. Finally, a linear relationship between the peak energy arrival time and the minimum propagation distance was established, universally holding true for all the types of cracks considered in this research. Moreover, the slope of the linear relationship is expected to vary with the diffusivity and dissipation coefficient.

The results of this research suggest that a preliminary knowledge of the cracking process is required to correctly interpret the measured impulse responses for an

unknown crack geometry, as the impulse response expresses only the response of the shortest path through a system of cracks between source and receiver. Moreover, the impulse response can carry some ambiguity, as for example shown by the non-vertical crack type. Furthermore, because of the linear relationship between the peak energy arrival time and the minimum propagation distance, the finite element method is suitable to generate look-up tables for rapid in-field evaluation of diffuse ultrasonic measurements.

5.1 Future Work

For a future research, more experimental validation of the simulation models is required in order to verify the simulation results and the quality of the model. Moreover, with the goal to model field applications, in a first step, the two-dimensional model should be adapted to have infinite elements (see Ansys documentation [2]) at the boundary, which would account for the absence of a spacial boundary in in-field applications. As a further step, a cracked three-dimensional model should be implemented and various crack configurations that are not available for two-dimensional models should be investigated and experimental validation should also be conducted. Furthermore, as a linear relationship between the peak energy arrival time and the minimum propagation distance was found, a sensitivity analysis of the influence of the diffusivity and dissipation coefficient on the slope of the linear fit should be established, with the goal of evaluating the feasibility of such a diagram as an in-field look-up table.

APPENDIX A

ADDITIONAL RESULTS FOR THE PARTIALLY CLOSED CRACKS

In this appendix, additional results from the simulations on the partially closed cracks are presented for the other two maximum crack depth subsets with $\delta_3 = 75mm$ and $\delta_3 = 100mm$, which are analyzed in this research. The analysis is analogues to the one presented in chapter four.

A.1 Maximum crack depth 75mm

Figure A.1 shows the peak energy arrival times for the configurations in table A.1 and compares these to the peak energy arrival times of vertical cracks with a depth of δ_1 or δ_3. It can be clearly seen from figure A.1 that the peak energy arrival time of the partially closed crack simulation matches that of the vertical crack with a depth of δ_1, indicating that the hidden part remains undetected by the simulation.

Table A.1: Simulation configurations for partially closed crack type with a total crack depth of 75 mm.

Configuration	1	2	3	4	5	6	7
D in m^2s^{-1}	10	10	10	10	10	10	10
σ in s^{-1}	21000	21000	21000	21000	21000	21000	21000
$2d$ in mm	60	60	60	60	60	60	60
δ_1 in mm	10	30	50	60	70	80	90
δ_2 in mm	20	50	70	80	90	95	100
δ_3 in mm	75	75	75	75	75	75	75

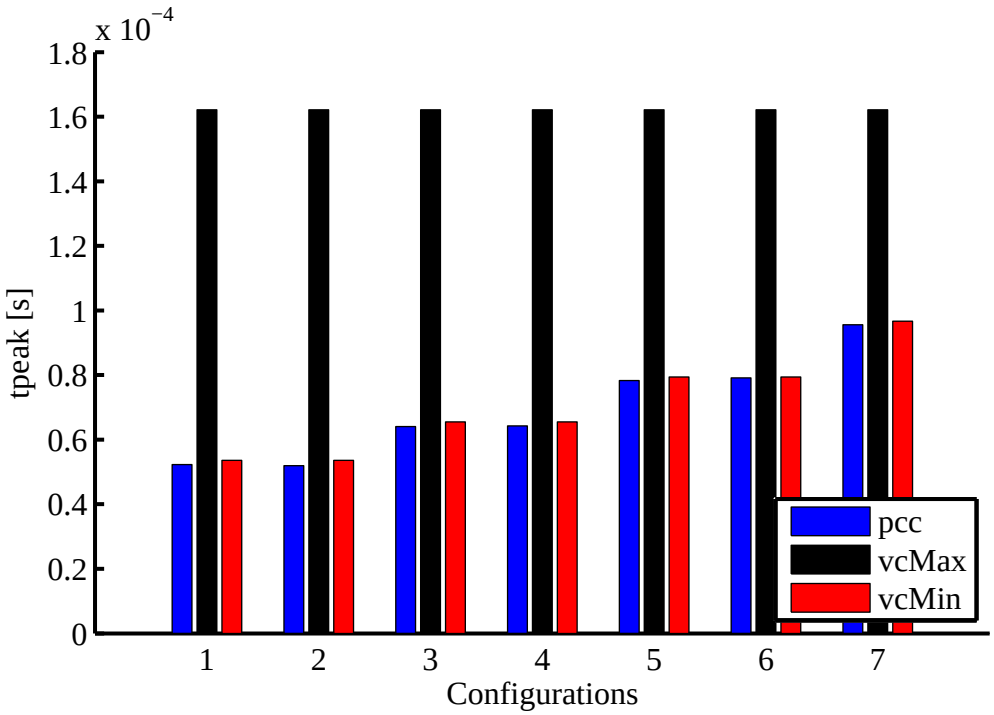

Figure A.1: Peak energy arrival time for all the configurations of table A.1 of the partially closed crack type with a total crack depth $\delta_3 = 75mm$.

A.2 Maximum crack depth 100mm

Figure A.2 shows the peak energy arrival times for the configurations of table A.2 and compares these to the peak energy arrival times of vertical cracks with a depth of δ_1 and δ_3. It is clearly seen from figure A.2 that the peak energy arrival time

Table A.2: Simulation configurations for partially closed crack type with a total crack depth of 100 mm.

Configuration	1	2	3	4	5	6	7
D in m^2s^{-1}	10	10	10	10	10	10	10
σ in s^{-1}	21000	21000	21000	21000	21000	21000	21000
$2d$ in mm	60	60	60	60	60	60	60
δ_1 in mm	10	30	50	60	70	80	90
δ_2 in mm	20	50	70	80	90	95	100
δ_3 in mm	100	100	100	100	100	100	100

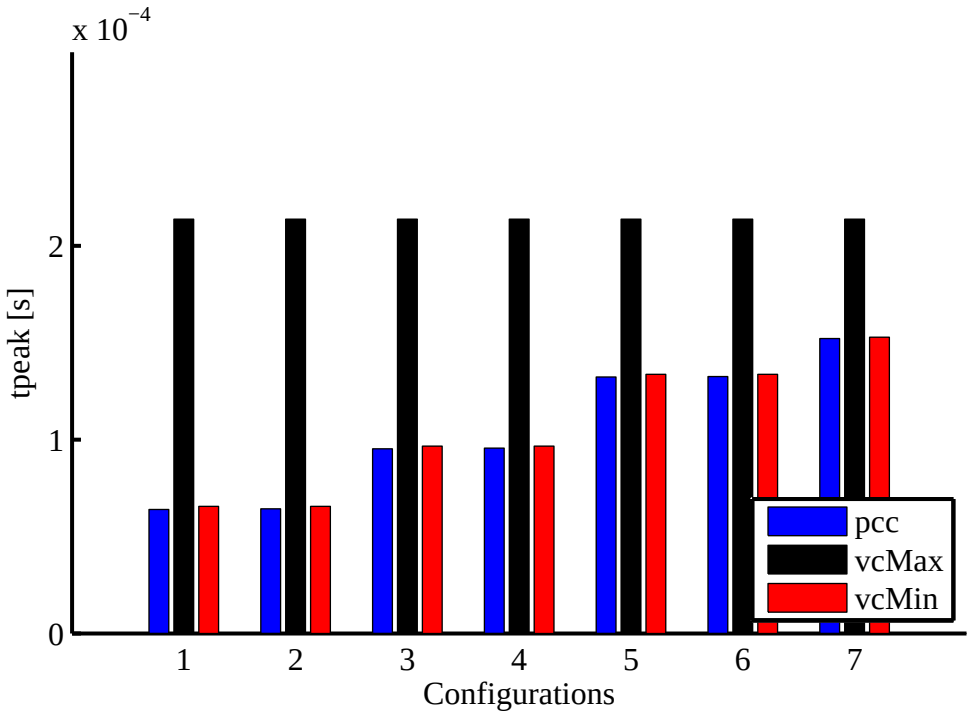

Figure A.2: Peak energy arrival time for all the configurations of table A.2 of the partially closed crack type with a total crack depth $\delta_3 = 100mm$.

of the partially closed crack simulation matches that of the vertical crack with a depth of δ_1, also indicating that the hidden part remains undetected by the simulated measurements.

APPENDIX B

ADDITIONAL RESULTS FOR THE NON-VERTICAL CRACKS

In this appendix, the energy curves for the other source-reciever distances $2d$ for the configurations in table 4.4 are presented in order to give more evidence to the argument made in chapter four.

B.1 Source-receiver distance 70mm

Figure B.1 shows the energy curves for a source-receiver distance of $2d = 70mm$. It is observed that the impulse response for the comparison of a positive angle with its

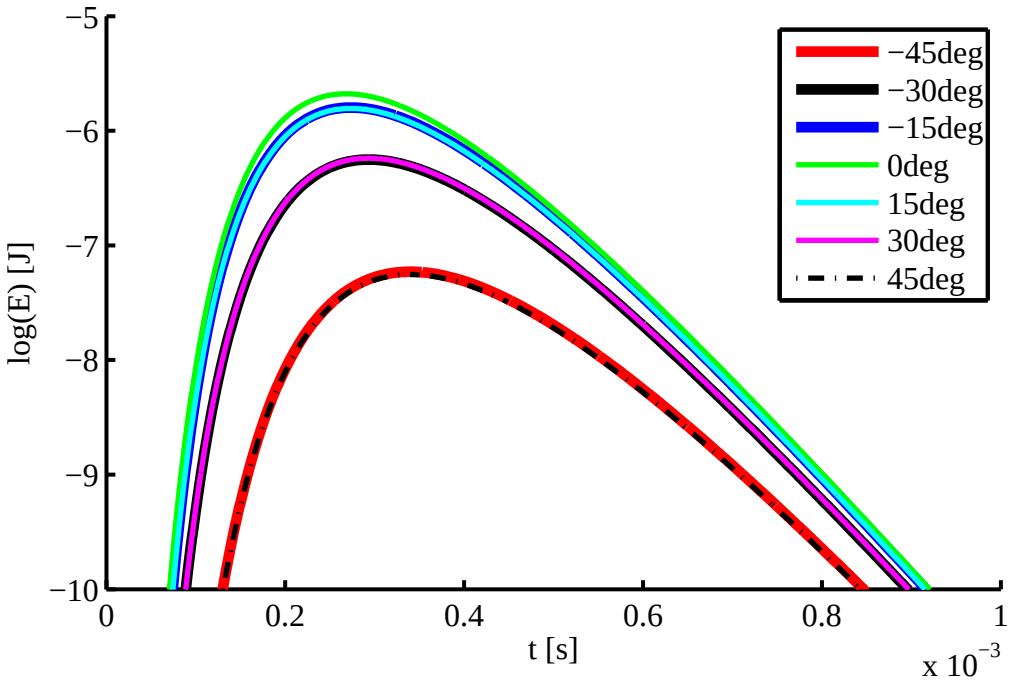

Figure B.1: Comparison of the energy curves for the non-vertical crack crack type at a source-receiver distance of $2d = 70mm$ in dependence on the angle α.

respective negative angle match yielding the ambiguity of the simulated measurements as discussed in chapter four.

B.2 Source-receiver distance 80mm

Figure B.2 shows the energy evolution curves for a source-receiver distance of $2d = 80mm$. It is observed, that the impulse response for the comparison of a positive angle with its respective negative angle match yielding the ambiguity of the simulated measurements as discussed in chapter fur.

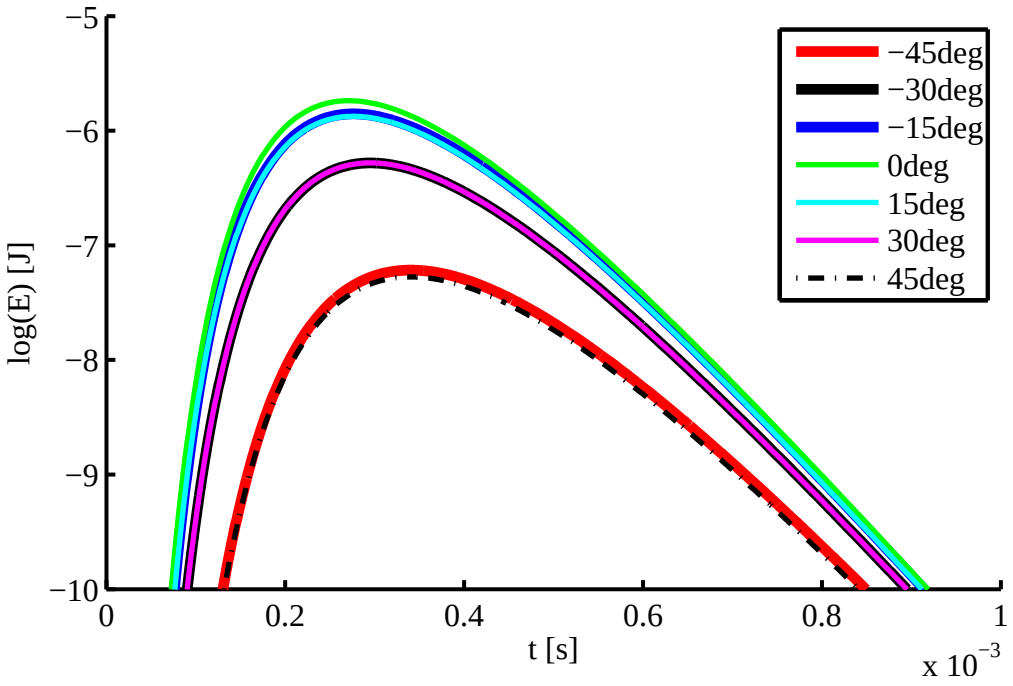

Figure B.2: Comparison of the energy curves for the non-vertical crack crack type at a source-receiver distance of $2d = 80mm$ in dependence on the angle α.

B.3 Source-receiver distance 90mm

Figure B.3 shows the energy evolution curves for a source-receiver distance of $2d = 90mm$. It is observed that the impulse response for the comparison of a positive angle with its respective negative angle match yielding the ambiguity of the simulated measurements as discussed in chapter four.

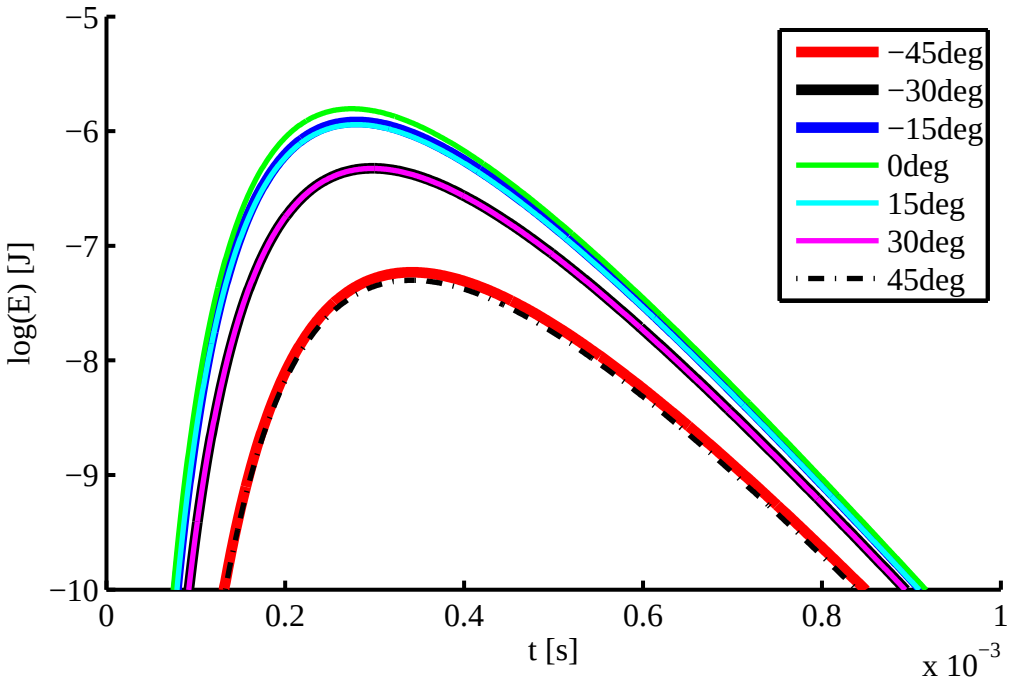

Figure B.3: Comparison of the energy curves for the non-vertical crack crack type at a source-receiver distance of $2d = 90mm$ in dependence on the angle α.

B.4 Source-receiver distance 100mm

Figure B.4 shows the energy evolution curves for a source-receiver distance of $2d = 100mm$. It is observed that the impulse response for the comparison of a positive angle with its respective negative angle match yielding the ambiguity of the simulated measurements as discussed in chapter four.

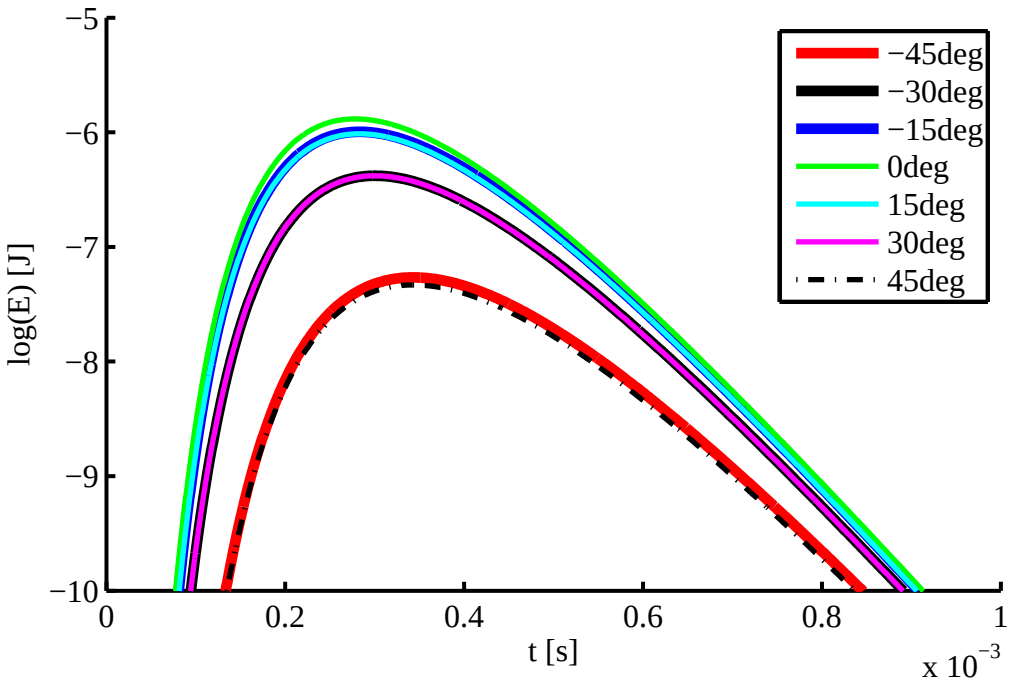

Figure B.4: Comparison of the energy curves for the non-vertical crack crack type at a source-receiver distance of $2d = 100mm$ in dependence on the angle α.

REFERENCES

[1] Achenbach, J., *Wave propagation in elastic solids*. North-Holland series in applied mathematics and mechanics, North-Holland Pub. Co., 1973.

[2] Ansys, *Ansys 13.0 Documentation*. Ansys Inc., 2010.

[3] Anugonda, P., Wiehn, J. S., and Turner, J. A., "Diffusion of ultrasound in concrete," *Ultrasonics*, vol. 39, pp. 429–435, Oct. 2001.

[4] Bathe, K., *Finite element procedures*. Prentice Hall, 1996.

[5] Becker, J., Jacobs, L. J., and Qu, J. M., "Characterization of cement-based materials using diffuse ultrasound," *Journal of Engineering Mechanics-asce*, vol. 129, pp. 1478–1484, Dec. 2003.

[6] Cowan, M. L., Beaty, K., Page, J. H., Liu, Z. Y., and Sheng, P., "Group velocity of acoustic waves in strongly scattering media: Dependence on the volume fraction of scatterers," *Physical Review E*, vol. 58, pp. 6626–6636, Nov. 1998.

[7] Deroo, F., Kim, J. Y., Qu, J. M., Sabra, K., and Jacobs, L. J., "Detection of damage in concrete using diffuse ultrasound (l)," *Journal of the Acoustical Society of America*, vol. 127, pp. 3315–3318, June 2010.

[8] Deroo, F., "Damage detection in concrete using diffuse ultrasound measurements and an effective medium theory for wave propagation in multi-phase materials," Master's thesis, Civil and Environmental Engineering, Georgia Institute of Technology, 2009.

[9] Graff, K., *Wave motion in elastic solids*. Dover books on engineering, Dover Publications, 1975.

[10] In, C., Kim, J. Y., Kurtis, K., and Jacobs, L., "Crack depth measurement in concrete using diffuse ultrasound," in *Review of Progress in Quantitative Nondestructive Evaluation*, 2011.

[11] Mandelis, A., *Diffusion-wave fields: mathematical methods and Green functions*. Springer, 2001.

[12] Mills, A., *Heat transfer*. Prentice Hall, 1999.

[13] Page, J. H., Schriemer, H. P., Bailey, A. E., and Weitz, D. A., "Experimental test of the diffusion approximation for multiply scattered sound," *Phys. Rev. E*, vol. 52, pp. 3106–, Sept. 1995.

[14] Ramamoorthy, S. K., Kane, Y., and Turner, J. A., "Ultrasound diffusion for crack depth determination in concrete," *Journal of the Acoustical Society of America*, vol. 115, pp. 523–529, Feb. 2004.

[15] Reddy, J., *An introduction to the finite element method*. McGraw-Hill series in mechanical engineering, McGraw-Hill Higher Education, 2006.

[16] Sheng, P., *Introduction to wave scattering, localization and mesoscopic phenomena*. Springer series in materials science, Springer, 2006.

[17] Weaver, R., "Ultrasonics in an aluminum foam," *Ultrasonics*, vol. 36, no. 1-5, pp. 435 – 442, 1998. Ultrasonics International 1997.

[18] Zhang, Z. Q., Jones, I. P., Schriemer, H. P., Page, J. H., Weitz, D. A., and Sheng, P., "Wave transport in random media: The ballistic to diffusive transition," *Phys. Rev. E*, vol. 60, pp. 4843–, Oct. 1999.